Investigating the effect of seismicity on spatial sediment sources and loads using the fingerprinting approach

Nafiseh Ashtari[a], Kazem Nosrati[a,*], Salma Ommi[b], Adrian L. Collins[c]

[a] *Department of Physical Geography, Faculty of Earth Sciences, Shahid Beheshti University, 1983969411 Tehran, Iran*

b Department of Environmental Planning and Design, Environmental Science Research Institute, Shahid Beheshti University, 1983969411, Tehran, Iran

[c] *Net Zero and Resilient Farming, Rothamsted Research, North Wyke, Okehampton, EX20 2SB, UK*

[*] **Corresponding author:**

Kazem Nosrati

Tel.: +98 21 29902604

Fax: +98 21 22431690

e-mail: k_nosrati@sbu.ac.ir

Abstract

Elevated soil erosion and suspended sediment loss are some of the most severe environmental problems in the river catchments of Iran. Seismic activity is known to elevate sediment loss and this study investigated sediment sources and loads in the Talar Drainage Basin in Iran, in the context of earthquake frequency and magnitude. A catalogue of earthquakes in the study region was assembled to estimate the expected high-frequency ground motions (i.e., Peak Ground Acceleration (PGA)). The horizontal ground acceleration was estimated using five global and reginal attenuation relationships to fingerprint sub-basin spatial sediment sources in the study area. Two size fractions (< 63 μm and 63–125 μm) and 49 geochemical elements were analysed on 30 sediment samples collected from three potential tributary sub-basin spatial sediment sources and 10 target sediment samples collected at the overall basin outlet. Source contributions were estimated using a Bayesian un-mixing model. The estimated relative contributions of the individual spatial sediment sources for both the <63 μm fraction (51.9% (48.6-55.3), 48 % (44.6-51.3), and 0. 1% (0-0.2)) and 63–125-μm fraction (68.2% (66.4- 69.8), 31.7% (30.1- 33.6), and 0.1 % (0-0.2)) correlated with recorded seismic events. The correlations between sub-basin specific sediment loads and PGA were r = 0.68 for the <63 μm fraction and r = 0.99 for the 63–125 μm fraction. The results demonstrate that seismic activity and ground acceleration can elevate erosivity and erodibility factors. This study supports environmental planners for targeting management to reduce suspended sediment loads and preserve fluvial habitats.

Keywords: Fingerprinting; Sediment loss; Peak Ground Acceleration; Seismicity; Probabilistic Seismic Hazards Assessment

1. Introduction

Accelerated mobilization and delivery of fine-grained sediments is a global issue (Aiello et al., 2015) which reduces soil and water quality, transports sediment-associated contaminants, threatens ecosystem status and causes sedimentation in canals and water reservoirs (Nosrati, 2017; Owens et al., 2005; Zhou et al., 2019). One of the factors that increases sediment supply is seismic activity which increases weathering and susceptibility to erosion (Koons et al., 2012; Portenga and Bierman, 2011). Here, the peak ground acceleration provides an accurate measurement of the status seismicity of an area since it depends strongly on the frequency of large and small earthquakes (Vanmaercke et al., 2014a). Therefore, accounting for the impact of seismic hazards on sediment dynamics in watersheds is important where such hazards prevail. In this context, controlling and managing excess soil erosion and sediment delivery is important to reduce inputs into rivers (Minella et al., 2008) and these actions depend upon reliable identification of sediment sources for prioritizing managerial actions (Collins et al., 2012b; Walling, 2013). The fingerprinting approach (Collins et al., 2020; Collins et al., 2017; Walling et al., 2013) is a direct method widely used to identify sediment sources and their relative contributions and is based on the comparison of the characteristics or fingerprints of fine-grained target sediment and catchment sediment sources (Collins et al., 1997a; Pulley et al., 2015). There are two basic assumptions underpinning the fingerprinting approach, comprising: 1- only conservative tracers should be used in composite fingerprints, and; 2- composite fingerprints better discriminate potential sediment sources (Collins and Walling, 2004). Therefore applying conservation tests to select reliable tracers for the dominant particle size fractions in the target sediment and selection of a robust sampling strategy are important considerations in the application of sediment fingerprinting. Given the challenges of deploying a more traditional slope-based source sampling strategy in the mountainous study area, a tributary-based sampling strategy was deployed as a pragmatic alternative approach (Nosrati et al., 2018).

Previous studies have investigated the key factors that control erosion and sediment delivery, such as landslides or seismic landslides, tectonics and other seismic activity using the peak ground acceleration (PGA) index and inventories of rockslides (Antinao and Gosse, 2009; Dadson et al., 2004b; Golosov and Tsyplenkov, 2021; Hovius et al., 2011; Howarth et al., 2012; Malamud et al., 2004; Molnar et al., 2007; Vanmaercke et al., 2017; Vanmaercke et al., 2014a; Vanmaercke et al., 2014b; Vanmaercke et al., 2015). These studies have illustrated the significant effect of tectonic processes and factors on increasing erosion and sediment yields.

However, far fewer studies have investigated the effect of seismicity, especially PGA, as an independent factor in controlling erosion and sediment loads in river basins. Accordingly, in this new study, we investigated the effect of seismicity through PGA on sediment load in the Talar drainage basin, Iran. Previous work in this study area has examined land use change as a key control on fine-grained sediment dynamics, but not seismicity (Mohammadi et al., 2021; Zare et al., 2017). More specifically, this new work aimed to document seismic hazards probabilistically by calculating PGA with a probability of 10% over a return period of 50 years and then to study the effect of seismicity on spatial sediment sources and loads using a fingerprinting procedure incorporating a Bayesian un-mixing model for source apportionment.

2. Materials and methods

2.1. Study area

The Talar study catchment (2105 km$^{2)}$ (latitude N-35 to N-36 and longitude 52_E to 53_E) lies in the central Alborz Mountains and on both sides of the Tehran-Ghaemshahr Road in Iran (Fig. 1). The main formations in the study area are Shemshak, Elika, Karaj, Lar with sandstone, conglomerate, dolomitic limestone, marl and shale lithologies (Fig. 1). The main and active faults in the Talar watershed, are IRQ 112 and IRQ 357. The main land use types comprise cultivated lands and orchards (80.8 km^2, 3.9%), rangelands (730.9 km^2, 34.7%), forests (1280.5 km^2, 60.8%), and residential areas (12.8 km^2, 0.6%). Mountainous topography dominates with elevations of 215 m to 3910 m a.s.l. and a mean slope of 20^o. Soils are mainly Mollisols, Entisols, Alfisols, and Inceptisols (Iran Forests, Range and Watershed Management Organization; IFRWMO). Long-term (1970-2020) mean annual precipitation is 1056 mm, and most rainfall occurs in October, the most humid month of the year. Local river drainage has dendritic and parallel patterns. The main channel is 100 km long, and the minimum slope is

1.7%, with a corresponding maximum of 18.3%. Mean annual discharge is 9.3 $m^3 s^{-1}$ based on a 50-year record (1970-2020) from the hydrometric station at the catchment outlet. Fifty-year (1970-2020) mean annual temperature is 13.7 ° C. Based on the 50-year (1970-2020) hydro-sedimentological record, the mean annual suspended sediment export is estimated at 15547 tonnes $year^{-1}$ (Iran Forests, Range and Watershed Management Organization; IFRWMO). Detailed information about each sub-basin is as follows: the average elevation above sea level of sub-basins 1, 2 and 3 are 2121.2 m, 1965.9 m, and 989.0 m, respectively. The areas of sub-basins 1, 2 and 3 are 1074.2 km^2, 559.9 km^2, and 336.2 km^2, and the average slopes (degrees) are 22.4, 23.3, and 18.3, respectively. The areas of the main geology units in sub-basin 1 are 310.9 km^2, 310.2 km^2, 430 km^2 and 23.5 km^2 for marl and shale, limestone and dolomite, sandstone and conglomerate, and Quaternary sediments, respectively, compared with 9.0 km^2, 105.9 km^2, 444.5 km^2, and 0.5 km^2 for sub-basin 2 and 128.8 km^2, 26.1 km^2, 180.5 km^2, and 0.7 km^2 for sub-basin 3. The main land use types comprise cultivated lands and orchards, rangelands, forests, and residential areas, with corresponding areas of 48.3 km^2, 692.5 km^2, 329.7 km^2 and 3.7 km^2 in sub-basin 1, 16.9 km^2, 126.8 km^2, 413.8 km^2 and 2.4 km^2 in sub-basin 2, and11.02, km^2,9.03 km^2, 314.3 km^2 and 1.8 km^2 in sub-basin 3.

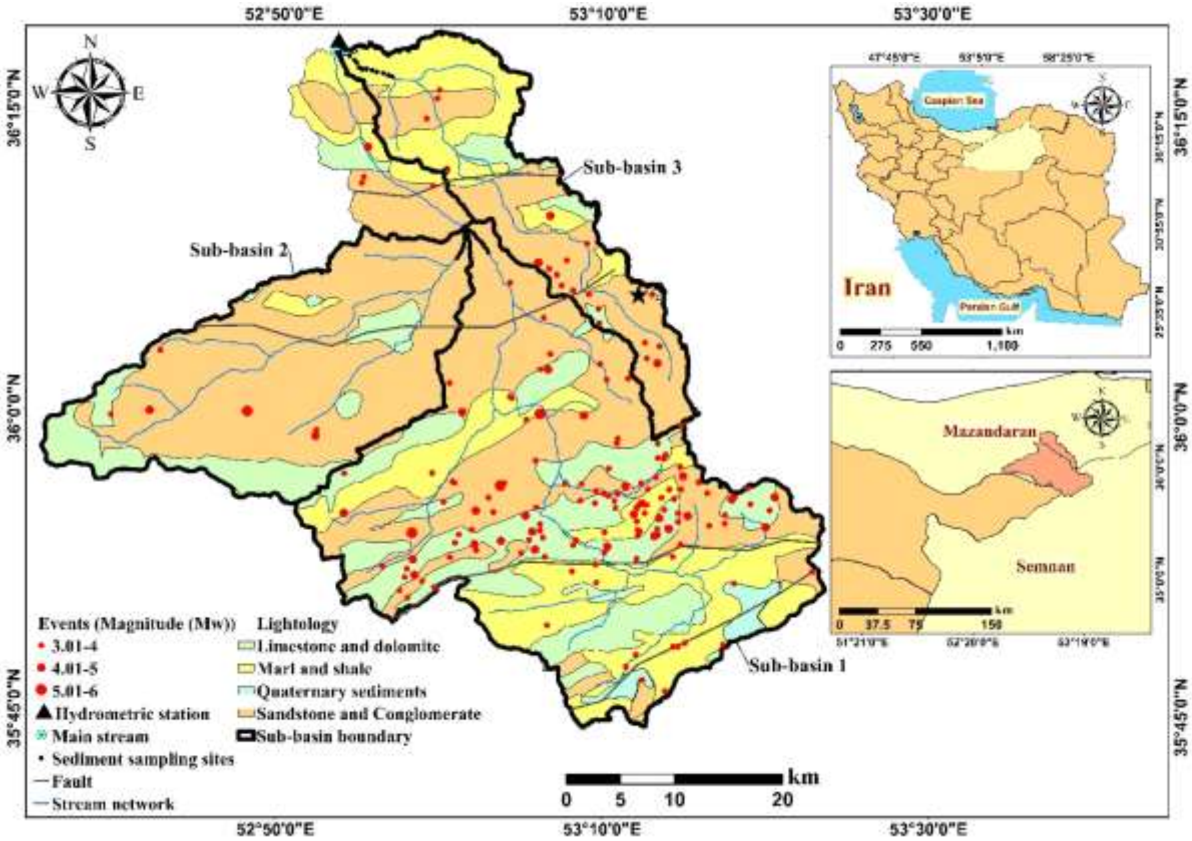

Fig. 1. Location of the Talar drainage basin in Iran, the main geological units and seismic status of the Talar for the period 5.3.1935 to 26.11.2020. The black star shows the historical earthquake of AD 1301. Locations of earthquakes extracted from the IIEES (International Institute of Earthquake Engineering and Seismology), IGUT (Institute of Geophysics of the University of Tehran) and (Berberian, 1994) catalogues.

2.2. Method for seismic hazard assessment

The probabilistic seismic hazard assessment method (PSHA) was used to determine the level of ground motion at a given place (Cornell, 1968; Cornell et al., 1971; McGuire, 1976). To analyze and assess seismic hazards and determine the response of each basin area, it is necessary to study the seismicity trend in the basin in question (Eluyemi et al., 2020). Therefore, the first step is to present a homogeneous catalogue (Ommi and Zafarani, 2016).

Earthquake catalogues were sourced from the Institute of Geophysics, Tehran University (IGUT) and the International Institute of Seismology and Earthquake Engineering (IIEES). These document the date and time of occurrence, the geographical coordinates, the epicenter distance, the focal depth, and the earthquake magnitude. The earthquake catalogue shows that a total of 36 earthquakes occurred with magnitudes ranging between 4.01 and $6 = M_w$. In total, 187 earthquakes occurred between 5.3.1935 and 26.11.2020. The largest historical earthquake in the study basin was recorded in AD 1301 with a magnitude of M_w=6.6 (Berberian, 1994) Fig. 1. The largest monitored earthquake in the basin was recorded on the January 20th 1990, with a magnitude $M_w = 6$.

The magnitude scale used in this study is M_w. Shahvar's regional relations were used to homogenize the catalogue (Shahvar et al., 2013). Estimation of the magnitude threshold should focus on the magnitude of completeness (MC), which is very important in seismicity studies because a maximum number of available events should be considered in order to achieve a reliable result. The MC shows the uniformity of the data, and in addition, the magnitudes that are greater than the MC are accurate (Ommi and Zafarani, 2016). This study applied the magnitude of completeness by the moving window method (Wiemer and Wyss, 2000). Removal of foreshocks and aftershocks from the earthquake catalogue was undertaken using the Gardner and Nopoff temporal and spatial window method (Gardner and Knopoff, 1974). The removal of non-Poissonian events was undertaken using zmap software.

The Gutenberg-Richter law (Eq. 1) was used to assess earthquake frequency. In fact, the Gutenberg–Richter frequency–magnitude relationship describes the earthquake activity in a particular region (Monterroso Juárez, 2003).

$$\log \lambda_m = a - b.m \tag{1}$$

in which a and b are the seismicity parameters: a indicates the mean annual number of earthquakes with magnitude greater than or equal to zero (a is a measure of the level of seismicity); b represents the seismicity changes, i.e., the ratio of small to large earthquakes (Kijko and Smit, 2012); m is the magnitude of the earthquake, and the λ_m is the annual rate of the mean of the earthquake of magnitude M (Gutenberg and Richter, 1944). An increase in the value of b indicates a decrease in the number of large earthquakes, and a reduction in the value of b shows seismic quiescence and an increase in seismic potential (Nuannin et al., 2005; Ommi and Zafarani, 2016; Tsukakoshi and Shimazaki, 2008; Wiemer and Wyss, 1997; Wu and Chiao, 2006).

By calculating coefficients of the relationship represented in the Gutenberg-Richter law, it is possible to assess the level of seismicity in a region (Ommi and Zafarani, 2016; Schorlemmer et al., 2003; Smith, 1981; Wyss and Stefansson, 2006). In particular, it is possible to estimate the maximum probable earthquake magnitude. In the probabilistic approach, the value of the maximum magnitude is estimated purely from the seismic background of the region, using the catalogue of seismic events and appropriate statistical approaches. (Choi et al., 2014; Kijko and Sellevoll, 1992; Salamat et al., 2019) and this can be used for earthquake hazard analysis (Cornell, 1968; Vahidifard et al., 2017; Zarrineghbal et al., 2021). Taking advantage of the Bayesian theorem in total probabilities, this approach calculates the probability distribution of potential hazards due to all existent active sources (within a given radius) for a study area (Cornell, 1968).

First, the cumulative distribution function of the occurrence of earthquakes larger than a magnitude of at least m_{min} is derived using Eq. (2):

$$F_M(m) = P(M \leq m | m_{max} > M > m_{min}) = \frac{N_{m_{min}} - N_m}{N_{m_{min}} - N_{m_{max}}} = \frac{\lambda_{m_{min}} - \lambda_m}{\lambda_{m_{min}} - \lambda_{m_{max}}} = C(1 - e^{-\beta(m - m_{min})}$$

$$m_{max} > m > m_{min} \quad (2)$$

in which $F_M(m)$ is a cumulative distribution function of earthquake magnitudes, m is the magnitude of the earthquake, N_m is the number of earthquakes in the catalogue, $N_{m_{min}}$ is the number of earthquakes with minimum magnitude, $N_{m_{max}}$ is the number of earthquakes with maximum magnitude, the λ_m is the annual rate of the mean of the events of the earthquakes of magnitude M, $\lambda_{m_{min}}$ is the rate of earthquakes with minimum magnitude, $\lambda_{m_{max}}$ is the rate of earthquakes with maximum magnitude, $\beta = b\, ln\, 10$ times the Richter b-value for the fault (the parameter b is typically such that β is about 1.5 to 2.3), and the coefficient C (Eq. 3) is applied to limit m to the maximum magnitude (m_{max}) derived from the cumulative distribution function.

$$C = \frac{1}{1-e^{-\beta(m_{max}-m_{min})}} \tag{3}$$

The probability density function ($f_M(m)$) is calculated using Eq. (4):

$$f_M(m) = C\beta e^{-\beta(m-m_{min})} \qquad m_{max} > m > m_{min} \tag{4}$$

The probability density function of the distance to the site ($f_R(r)$), is obtained by dividing each seismic source into smaller parts, measuring each component's distance from the site, and using the corresponding frequency.

Using the probability density function of the magnitude of each source ($f_M(m)$), the probability density function of the distance to the site ($f_R(r)$), and the probability density function of the occurrence of different levels of seismic intensity with magnitude m occurring at a distance r from the site, $P(IM > x)|m,r)$, the probability of exceedance of the ground motion parameter can be obtained using Eq. (5):

$$P(IM > x) = \sum_{i=1}^{n_{sources}} \lambda(M_i > m_{min}) \int_{m_{min}}^{m_{max}} \int_0^{r_{max}} P(IM > x)|m,r) f_{M_i}(m) f_{R_i}(r)\, dr\, dm \tag{5}$$

In the above formula, $\lambda(M_i > m_{min})$ is the occurrence rate of earthquakes greater than m_{min} for the i source. $P(IM > x)$ is the probability of an annual occurrence of $IM > x$ where IM is the ground motion parameter. $n_{sources}$ is the number of sources. The expression $P(IM > x)|m,r)$ is obtained from an attenuation relationship. M_i and R_i denote the magnitude and distance distributions for source i (Cornell, 1968). A hazard curve is obtained by calculating the annual occurrence rate of different levels of the ground motion parameter using the above integration process and plotting the result.

As the number of recordings of strong ground motion increase, there has been a trend towards developing region-specific attenuation relationships rather than just using the global average models developed for the broad tectonic categories. Often, there is a tendency to over-emphasize region-specific data in developing region-specific attenuation (Lee et al., 2002).

To compute the probabilistic hazard analysis (PSHA) maps, five empirical equations for the prediction of PGA were used: 1) the Next Generation Attenuation (NGA) proposed by (Akkar and Bommer, 2010), 2) the method presented by Abrahamson et al. (2008), 3) the regional relationship proposed by Soghrat et al. (2012), 4) the equation from Sinaeian (Ghasemi et al., 2009b), and 5) the method proposed by Ghasemi et al. (2009a). Using a logic tree approach, the results of these five relationships were given equal weights and ranked. The result of the weighting calculations has been shown in Fig. 4. The map of the ground acceleration changes for the Talar drainage basin was estimated using a 50-years return period and an occurrence probability of 10%.

2.3. Field sampling and laboratory measurements

Fine-grained drape sediment samples on the riverbed were used as target sediment to discriminate the relative contribution from upstream sediment sources (Nosrati et al., 2018). Drape samples were also collected at the outlets of three tributary sub-basins which were used as potential spatial sediment sources (Fig. 2). The bed sediment samples that appeared to have been recently deposited were collected at each of the channel sampling sites after a rainfall-runoff event (23 August 2020). Sampling covered the main channel and three major tributaries in the study area (Fig. 1).

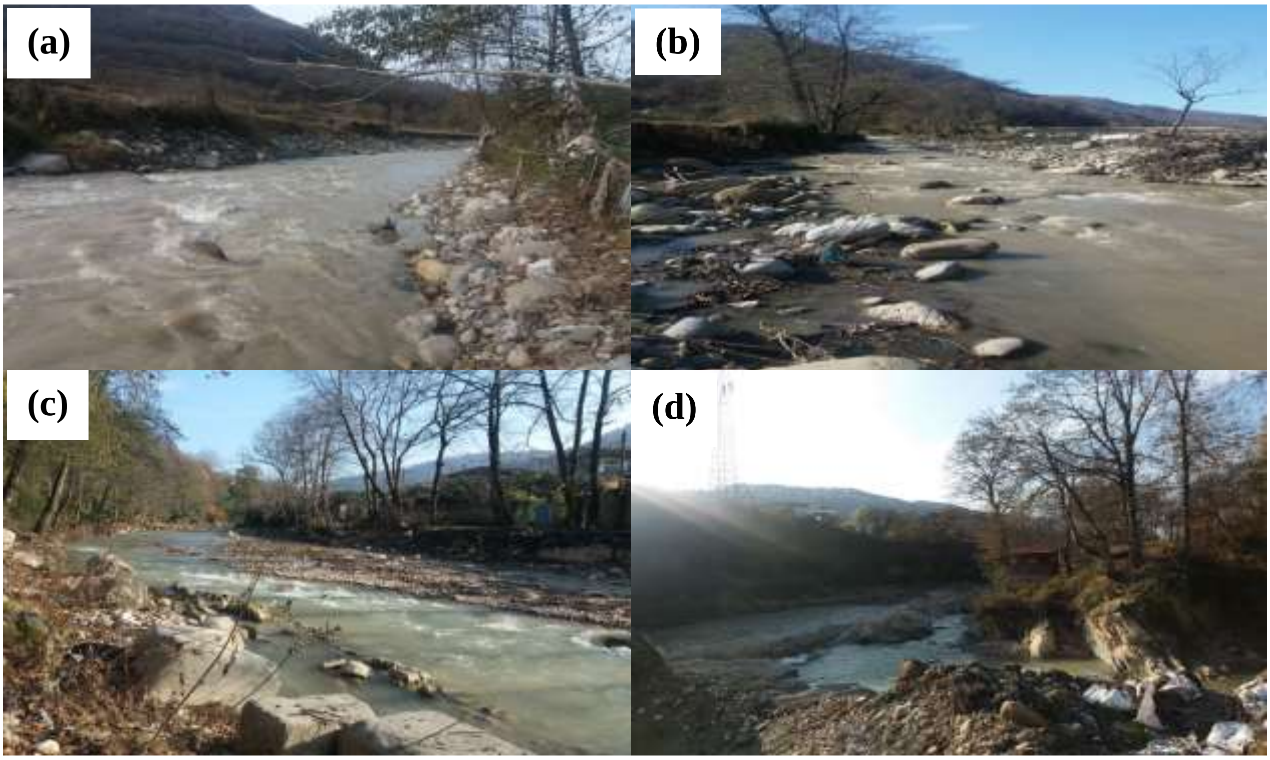

Fig. 2. Photos of the river sampling sites: (a) sub-basin 1 outlet; (b) sub-basin 2 outlet; (c) sub-basin 3 outlet, and; (d) the overall outlet of the study basin used for the collection of target sediment samples.

Each river bed drape sediment sample was a composite of 10 sub-samples collected at 100 m intervals in the corresponding outlet reach. Samples collected at the overall outlet of the study basin were used as target sediment for the spatial source apportionment (Nosrati et al., 2018). In total, ten composite samples were taken from the outlet of each of the three tributary sub-basins, and a further ten were collected from the overall outlet. The typical mass of each composite river bed drape sediment sample was ~500 g. After collection, the samples were air dried and manually disaggregated using a pestle and mortar. Since erosion has the potential to mobilize all particle sizes, it is necessary to determine the most representative particle size fractions for the tracer being deployed in both target sediment and source samples, since this helps ensure that the source and target sediment samples are directly comparable using the selected tracers. Accordingly, the particle size characteristics of the spatial source and target sediment samples was determined in the laboratory to identify the most appropriate size fractions for direct comparison of fingerprint properties (Pulley et al., 2015; Tiecher et al., 2018). Dry sieving showed that the most representative particle size fractions were the <63 μm fraction (51.7% of total sample mass) the 63–125 μm fraction (32.0% of total sample mass) (Fig. SI 1). On this basis, these two dominant particle size fractions were used in our study.

The concentrations of geochemical tracers (Al, As, Ba, Be, Bi, Ca, Ce, Co, Cr, Cs, Cu, Dy, Er, Eu, Fe, Gd, Hf, K, La, Li, Lu, Mg, Mn, Na, Nb, Nd, Ni, P, Pb, Pr, Rb, S, Sc, Si, Sm, Sn, Sr, Ta, Tb, Th, Ti, Tl, Tm, U, V, Y, Yb, Zn, Zr) were measured in both the <63 μm and 63-125 μm fractions of the samples using an Inductively Coupled Plasma mass spectrometer (ICP-MS) in the Zar Azma laboratory in Iran. Aqua regia (HCl–HNO_3; 3:1) and hydrofluoric acid were used to digest the disaggregated samples at 220 °C for four hours (Jenner et al., 1990). Typical analytical errors were <5% of the reported concentrations in milligrams per kilogram. The results of the geochemical analyses are summarized in Table 1.

2.4. Statistical tests and identification of composite fingerprints

Sediment tracers should behave conservatively during sediment transport through river basins (Lamba et al., 2015). Changes in particle size (Horowitz and Elrick, 1987; Motha et al., 2003) and organic matter content (Nadeu et al., 2011; Wang et al., 2010) cause non-conservative behaviour in sediment tracers during transportation and in conjunction with changes in environmental conditions (Taylor et al., 2013). For example, a 10% difference in the average concentration of a tracer in two non-conservative source groups, propagates errors into the final results (Pulley et al., 2017). For tracers to be able to deliver maximum discrimination between potential sediment sources using statistical tests, conservative behavior is important. Many studies show that identifying non-conservative tracers and removing them gives more accurate results (Nosrati et al., 2019). To identify non-conservative tracers, the concentrations of tracers in the target sediment samples collected at the overall main outlet were compared with the corresponding range measured on the river bed drape sediment samples collected to represent the tributary sub-basin spatial sources; i.e., a standard bracket or range test (Nosrati et al., 2019). Target sediment sample tracers that were not within the range of the concentrations measured on the sub-basin sediment samples were excluded from further consideration (Nosrati et al., 2018). Also a stricter conservation test known generally as the average concentration test was used by comparing the mean target sediment concentrations of the tracers with the corresponding means for the spatial sediment sources (Wilkinson et al., 2013). These tests provide a basis for screening and elimination of tracers that display substantial alteration in target sediment samples.

Robust discrimination between different potential sediment sources is an obligation in source fingerprinting. Multivariate statistical techniques comprising the Kruskal-Wallis H-test, discriminant function analysis (DFA), principal component analysis (PCA), principal components & classification analysis (PCCA), general classification & regression tree model (GCRTM), and cluster analysis, are commonly used to select composite fingerprints for source discrimination (Collins et al., 2012a; Nosrati et al., 2020; Nosrati and Collins, 2019a; Nosrati and Collins, 2019b; Palazón and Navas, 2017). Using the tracers passing the conservatism tests, two common statistical tests were used to identify final composite signatures for distinguishing the tributary sub-catchment spatial sediment sources: (1) the Kruskal-Wallis test (KW-H test), and (2) discriminant function analysis (DFA). The KW-H test compares more than two groups and tests the null hypothesis that the different groups are composed of distributions with equal means (Collins and Walling, 2002). Accordingly, the KW-H test removes any tracers that do not show statistically significant differences between the concentrations of the spatial sediment sources (Raigani et al., 2019). Tracers passing the KW-H test were entered into the discriminant function analysis. The DFA, using Wilks' lambda in a stepwise selection procedure, was used to determine the maximum discrimination between the spatial sediment sources on the basis of final composite fingerprints (Collins et al., 1997b; Evrard et al., 2011). All statistical analyzes were applied using STATISTICA V.8.0 (StatSoft, 2008).

2.5. Determination of the contributions of the spatial sediment sources

Moore and Semmens (2008) outlined a Bayesian framework for incorporation of prior information and uncertainty into stable isotope mixing models used in wildlife ecology. Nosrati et al. (2014) developed this model to apportion spatial sediment source contributions, generating the Modified MixSIR Bayesian model in Matlab. The Modified MixSIR model estimates the source contributions (f_i) using probability distributions of their proportional inputs to the target sediment samples. Based on the Bayes rule, it is assumed that the posterior probability distribution for all f_i is proportional to the prior probability distributions ($p(f_q)$) multiplied by the likelihood of the data given f_q, ($L(data|fq)$), and then dividing by their sum:

$$P(f_q|data) = \frac{L(data|f_q) \times p(f_q)}{\sum L(data|f_q) \times p(f_q)} \quad \text{Eq. 6}$$

Mean and variance parameters for each source i and the final composite fingerprint j were calculated and used to estimate corresponding probability distributions. Tracer distributions for target sediment samples were determined by solving for the proposed means $\hat{\mu}_j$ and standard deviations $\hat{\sigma}_j$ based on the randomly drawn f_i values comprising a vector f_q:

$$\hat{\mu}_j = \sum_{i=1}^{n} (f_i \times m_{j_{Source_i}}) \quad \text{Eq. 7}$$

$$\hat{\sigma}_j = \sqrt{\sum_{i=1}^{n} (f_i^2 \times S^2_{j_{Source_i}})} \qquad \text{Eq. 8}$$

where $m_{j_{Source_i}}$ is the mean and $S^2_{j_{Source_i}}$ is the variance of the jth target sediment sample tracer and the ith sediment source. Based on the $\hat{\mu}_j$ and $\hat{\sigma}_j$ of the composite fingerprint, the likelihood of the data given the proposed target sediment mixture is estimated using:

$$L(x|\hat{\mu}_j, \hat{\sigma}_j) = \prod_{k=1}^{n}\prod_{j=1}^{n}\left[\frac{1}{\hat{\sigma}_j \times \sqrt{2\times\pi}} \times \exp\left(-\frac{(X_{kj} - \hat{\mu}_j)^2}{2\times\hat{\sigma}_j^{\,2}}\right)\right] \qquad \text{Eq. 9}$$

where X_{kj} represents the j^{th} tracer property of the k^{th} target sediment sample. The model was run for 10^6 iterations for each of the final composite fingerprints generated using the DFA. Further details on this un-mixing model can be found in the aforementioned references.

3. Results

3.1. Determination of seismic parameters

The results showed that the values of seismicity parameters a and b in the Gutenberg-Richter law were 4.6 and 0.8, respectively (Fig. 3). The b value of <1, indicates that the study area is highly stressed in terms of seismicity. The maximum credible magnitude for an earthquake in the study area using the Gibowicz-Kijko (1994) method was estimated to be 6.5 ($\pm\sigma$ 0.4).

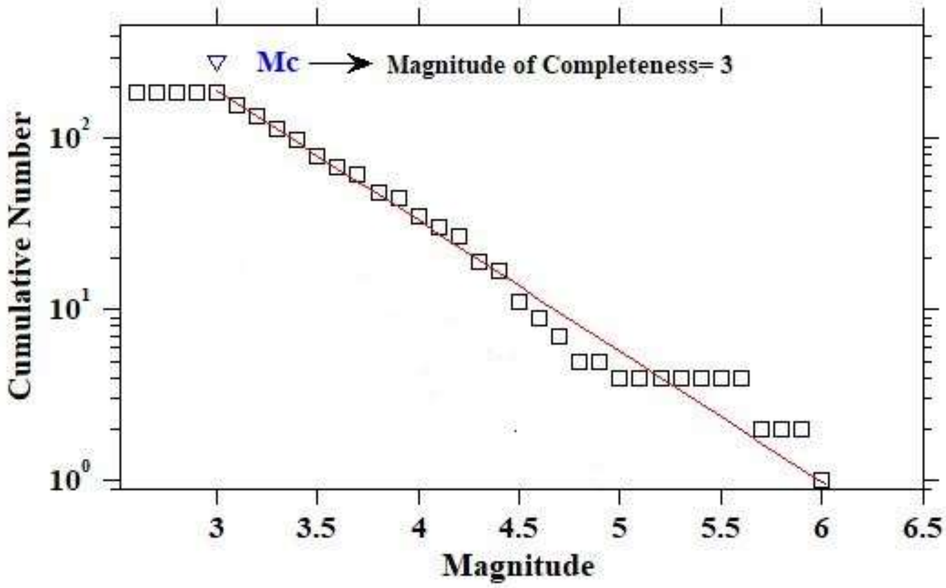

Fig. 3. Frequency– magnitude distribution for the Talar drainage basin earthquake catalogue.

3.2. Changes in peak ground acceleration

A map of horizontal peak ground motion changes was generated to estimate the seismic hazard (Fig. 4) in the Talar drainage basin, assuming a 10% probability of occurrence and a 50-year return period. The values for ground accelerations presented in Fig. 4 are coefficients of g (ground motion acceleration) and range between 0.3 and 0.6 g. Importantly, most of the study basin area is characterized by a moderate to high risk of ground acceleration in the range of 0.4 to 0.5 g. In some areas, this acceleration is even higher, with for example, maximum acceleration in tributary sub-basins 1 and 2 reaching 0.6 g. In sub-basin 3, the highest value is 0.6 g. The high values of PGA in sub-basin 1 are controlled by the Firuzkuh fault (IRQ357), by the IRQ112 fault in sub-basin 2 and by the IRQ 112 and North Alborz faults in sub-basin 3.

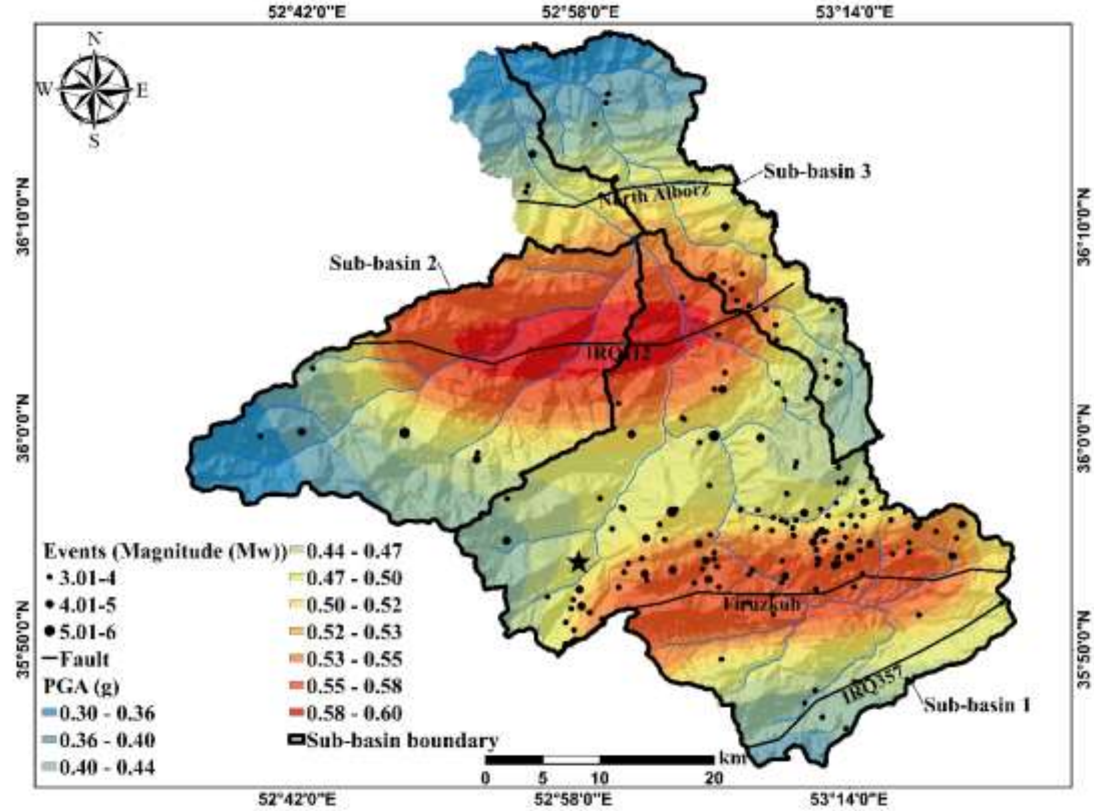

Fig. 4. Seismic hazard map (PGA) in the Talar drainage basin for a 50-year return period for the 10% probability. The black star shows the largest earthquake event of 1990 with M_w= 6.

3.3. Selecting composite fingerprints to discriminate spatial sediment sources

The results of the standard bracket test (or range test) for the <63 μm and 63–125 μm fractions showed evidence of non-conservative behaviour for 12 (As, Bi, Co, Cu, Fe, Mn, Ni, Pb, S, Sc, Sn, Y) and 27 (Al, Be, Co, Cs, Cu, Dy, Er, Eu, Fe, K, Mn, Nb, Ni, P, Rb, Sc, Sn, Ta, Tb, Th, Ti, Tl, U, V, Y, Yb, Zr) tracers, respectively. These were removed from subsequent data processing. Importantly, the average concentration test as a stricter conservatism test compared to the standard bracket test, also confirmed conservative behavior of the remaining tracers.

The results of the KW-H test (Table 1) suggested that of the remaining 37 conservative tracers for the <63 μm fraction and the remaining 22 such tracers for the 63–125 μm fraction, only U in the <63 µm fraction is not significant at a significance level of <0.05. Table 1 illustrates how with an increasing value of the H statistic, the level of statistical significance improves.

Table 1: Tracer concentrations in the spatial source and target sediment samples, results of the standard bracket test and KW-H test results for the <63 µm and 63–125 -µm fractions. Units for all elements are mg kg^{-1}.

Tracer		Spatial sediment sources						KW-H test		Target sediment samples	
		Sub-basin 1		Sub-basin 2		Sub-basin 3					
		Mean	SD	Mean	SD	Mean	SD	H value	p-Value	Mean	SD
< 63 µm fraction	Al	37254	4734.0	64687	6703.8	39798	4010.9	19.7	< 0.001*	54702	4321.7
	As	5.3	1.7	10.7	3.6	5.2	0.6	n.c.	n.c.	6.1	1.1
	Ba	314.3	31.1	365.8	33.3	280.8	11.6	20.1	< 0.001*	293.0	9.4
	Be	0.8	0.09	1.4	0.1	0.8	0.1	20.1	< 0.001*	1.1	0.1
	Bi	0.1	0.03	0.2	2.9	0.2	2.9	n.c.	n.c.	0.2	2.9
	Ca	149503	12132.6	23380	1572.6	102767	8499.1	25.8	< 0.001*	93292	14119.4
	Ce	45.2	4.1	69.4	6.8	55.8	5.9	22.3	< 0.001*	52.9	3.4
	Co	11.4	1.1	13.5	0.8	10.3	0.5	n.c.	n.c.	12.7	1.2
	Cr	80.0	4.1	102.7	3.5	83.9	6.2	19.8	< 0.001*	88.5	4.5
	Cs	2.1	0.3	3.4	0.3	2.4	0.3	20.3	< 0.001*	3.0	0.2
	Cu	21.8	1.7	30.6	3.6	19.1	1.4	n.c.	n.c.	37.3	10.4
	Dy	2.5	0.2	3.4	0.2	3.2	0.2	19.9	< 0.001*	3.0	0.2
	Er	1.3	0.1	2.0	0.1	1.8	0.08	24.5	< 0.001*	1.8	0.1
	Eu	0.6	0.05	1.0	0.1	1.0	0.04	19.3	< 0.001*	0.9	0.06
	Fe	26371	2475.5	39098	373.5	28738	822.3	n.c.	n.c.	36041	2816.8
	Gd	2.8	0.1	4.3	0.4	4.1	0.2	19.5	< 0.001*	3.7	0.1
	Hf	2.1	0.2	3.8	0.4	3.1	0.1	25.8	< 0.001*	2.9	0.1
	K	8908.2	785.9	14908.4	1459.1	11371.7	833.5	25.3	< 0.001*	12607.9	726.2
	La	24.5	2.1	34.0	2.7	30.4	1.9	22.6	< 0.001*	28.5	1.4
	Li	25.9	2.8	57.3	10.7	27.0	2.2	19.7	< 0.001*	41.0	3.7
	Lu	0.1	0.02	0.3	0.01	0.2	0.01	24.2	< 0.001*	0.2	0.03
	Mg	258.6	33.3	121	4.6	8561.1	339.4	25.8	< 0.001*	187.6	10.1
	Mn	526.7	66.1	585.8	55.2	637.2	13.0	n.c.	n.c.	631.3	41.8
	Na	5960.6	534.2	11234.8	677.5	5010.3	578.3	23.0	< 0.001*	7867.5	419.5
	Nb	10.6	0.7	15.4	1.3	12.6	0.7	24.5	< 0.001*	13.3	0.9
	Nd	16.3	1.6	25.5	2.7	25.9	2.0	19.3	< 0.001*	20.5	1.4
	Ni	33.9	1.9	37.4	3.1	30.6	2.5	n.c.	n.c.	37.8	2.2
	P	664.0	21.9	705.8	57.8	586.8	19.6	20.9	< 0.001*	682.4	20.7
	Pb	57.9	30.3	39.6	8.0	11.8	1.3	n.c.	n.c.	78.5	34.0
	Pr	3.2	0.4	6.0	0.5	6.1	0.7	19.3	< 0.001*	4.7	0.2
	Rb	29.7	3.4	60.9	7.6	45.1	3.4	24.3	< 0.001*	49.1	3.9
	S	685.1	77.8	980.2	723.1	599.8	48.1	n.c.	n.c.	588.5	24.2
	Sc	8.1	0.7	9.6	0.4	7.2	0.6	n.c.	n.c.	9.5	0.8
	Si	145008	17053.6	275838	7232.1	218189	6347.0	25.8	< 0.001*	208781	18617.3
	Sm	2.2	0.3	4.2	0.5	3.9	0.4	20.1	< 0.001*	3.3	0.2
	Sn	0.8	0.06	1.4	0.1	1.0	0.1	n.c.	n.c.	1.7	0.3
	Sr	285.7	26.3	132.0	7.7	196.6	5.2	25.8	< 0.001*	206.9	4.1

	Ta	0.6	0.05	1.0	0.06	0.9	0.1	20.6	< 0.001*	0.9	0.08
	Tb	0.4	0.03	0.6	0.07	0.5	0.03	19.8	< 0.001*	0.5	0.03
	Th	4.1	0.6	8.9	0.9	7.2	0.6	24.3	< 0.001*	6.5	0.5
	Ti	3726.7	188.7	5250.7	415.6	3954.5	164.5	21.9	< 0.001*	4299.1	196.2
	Tl	0.2	0.06	0.3	0.04	0.2	0.03	16.4	< 0.001*	0.3	0.03
	Tm	0.1	0.02	0.2	0.03	0.2	0.02	21.6	< 0.001*	0.2	0.01
	U	1.9	0.03	2.0	0.2	1.8	0.1	2.7	0.2	1.9	0.08
	V	74.7	4.8	93.2	7.06	70.4	2.6	20.2	< 0.001*	86.1	5.3
	Y	19.9	1.2	19.9	1.2	19.9	0.7	n.c.	n.c.	21.2	1.2
	Yb	2.2	0.08	1.8	0.04	2.0	0.07	25.2	< 0.001*	2.1	0.09
	Zn	143.3	6.2	77.9	6.6	56.5	4.0	25.8	< 0.001*	113.7	7.6
	Zr	79.9	11.5	125.3	9.1	91.7	7.6	21.5	< 0.001*	93.4	5.9
63–125 µm fraction	Al	38023	4236.8	55664	2627.8	25992	2511.2	n.c.	n.c.	53622	5358.9
	As	5.1	0.8	10.6	2.8	3.5	0.4	25.1	< 0.001*	5.7	1.3
	Ba	336.9	56.6	363.5	63.4	229.5	13.3	19.4	< 0.001*	288.9	11.8
	Be	0.7	0.05	1.1	0.0٧	0.5	0.1	n.c.	n.c.	1.1	0.1
	Bi	0.2	0.1	0.2	2.9	0.1	0.04	7.8	0.02*	0.2	2.9
	Ca	144242	20905.1	25556	1840.8	101079	6090.2	25.5	< 0.001*	85789	7031.3
	Ce	41.8	3.3	56.3	4.9	49.0	3.6	21.3	< 0.001*	51.1	3.3
	Co	11.9	0.5	11.8	0.7	6.8	0.8	n.c.	n.c.	13.0	1.1
	Cr	87.3	13.3	79.3	7.2	52.6	6.2	20.1	< 0.001*	80.2	9.2
	Cs	1.9	0.3	2.9	0.2	1.4	0.2	n.c.	n.c.	3.2	0.4
	Cu	19.4	1.7	26.5	1.4	12.0	1.2	n.c.	n.c.	29.7	2.6
	Dy	2.3	0.2	3.1	0.1	2.7	0.1	n.c.	n.c.	3.1	0.2
	Er	1.7	0.9	1.7	0.08	1.5	0.04	n.c.	n.c.	1.9	0.3
	Eu	0.7	0.08	0.9	0.06	1.0	0.08	n.c.	n.c.	0.9	0.08
	Fe	30271	1651.3	35399	1587.0	20573	831.4	n.c.	n.c.	34068	2592.0
	Gd	2.9	0.2	3.9	0.3	3.8	0.2	19.2	< 0.001*	3.8	0.2
	Hf	2.1	0.1	3.2	0.1	2.1	0.1	19.5	< 0.001*	2.7	0.3
	K	8468.9	805.9	12289.5	844.4	8269.0	742.5	n.c.	n.c.	12216.9	1107.6
	La	23.0	1.4	27.8	3.3	27.1	1.7	14.5	< 0.001*	27.1	1.8
	Li	24.3	2.7	49.3	6.7	17.8	2.1	25.8	< 0.001*	41.6	4.7
	Lu	0.1	0.03	0.2	0.02	0.1	0.0٠8	16.5	< 0.001*	0.2	0.02
	Mg	242.4	14.0	112.8	5.0	5746.2	582.9	25.8	< 0.001*	163	6.3
	Mn	570.6	32.3	544.3	40.2	468.9	26.0	n.c.	n.c.	676.8	51.4
	Na	5924.5	560.2	11664.3	721.0	4286.1	251.2	25.8	< 0.001*	7435.3	317.3
	Nb	9.0	0.9	12.8	0.5	11.3	0.7	n.c.	n.c.	12.2	1.9
	Nd	16.4	1.9	24.2	2.2	25.4	1.8	20.1	< 0.001*	22.0	1.2
	Ni	36.1	1.3	33.4	1.2	19.4	2.2	n.c.	n.c.	38.2	4.1
	P	582.6	12.207	530.0	19.2	455.6	26.9	n.c.	n.c.	634.6	44.4
	Pb	50.5	24.4	57.1	24.3	8.1	1.9	19.5	< 0.001*	45.0	11.6
	Pr	3.5	0.5	5.6	0.6	6.3	0.6	20.7	< 0.001*	5.0	0.4
	Rb	28.9	4.1	51.0	2.7	30.0	3.0	n.c.	n.c.	50.9	5.9
	S	602.3	25.7	818.1	419.7	499.3	42.9	11.1	0.003*	671.4	86.2
	Sc	7.9	0.3	7.8	0.3	4.6	0.5	n.c.	n.c.	9.3	1.0
	Si	173018	7888.5	276905	10318.2	252110	10246.4	25.3	< 0.001*	209804	6771.3
	Sm	2.3	0.4	3.6	0.6	3.9	0.5	17.6	< 0.001*	3.4	0.1
	Sn	0.8	0.09	1.2	0.08	0.7	0.0	n.c.	n.c.	1.4	0.1
	Sr	244.1	6.5	119.6	2.2	182.1	7.9	25.8	< 0.001*	206.6	1.6
	Ta	0.6	0.03	0.9	0.04	0.7	0.1	n.c.	n.c.	0.9	0.06
	Tb	0.4	0.03	0.5	0.02	0.5	0.02	n.c.	n.c.	0.5	0.04
	Th	4.0	0.7	7.7	0.4	4.7	0.3	n.c.	n.c.	6.5	1.0
	Ti	3468.4	150.9	4150.9	156.0	3314.4	165.6	n.c.	n.c.	3969.0	340.1
	Tl	0.2	0.07	0.3	0.01	0.1	0.02	n.c.	n.c.	0.3	0.04
	Tm	0.1	0.01	0.2	0.02	0.2	0.09	13.0	< 0.001*	0.2	0.01

	U	1.8	0.1	1.7	0.1	1.3	0.04	n.c.	n.c.	2.0	0.1
	V	71.6	2.0	76.3	2.1	49.9	3.4	n.c.	n.c.	85.3	11.0
	Y	16.9	0.4	15.9	0.7	15.0	0.9	n.c.	n.c.	19.8	1.6
	Yb	2	0	1.4	0.05	1.5	0.05	n.c.	n.c.	1.9	0.1
	Zn	123.0	6.6	68.2	3.7	35.9	4.8	25.8	< 0.001*	103.8	7.6
	Zr	61.9	4.8	82.9	6.6	51.6	10.3	n.c.	n.c.	82.7	12.6

* Critical p-value = 0.05 and n.c.-= non-conservative tracer on the basis of the bracket test

The second step in selecting final composite fingerprints involved the use of DFA. Among the 36 tracers that passed the KW-H test for the <63 µm fraction, and the 22 tracers that passed for the 63–125 µm fraction, the final composite fingerprint for the <63 µm fraction included five tracers (Al, Ba, Mg, Sr, Zn) and four tracers (Mg, Na, Sr, Zn) for the 63–125 µm fraction (Table 2). The results in Table 2 show the progressive percentage of source samples classified correctly at each step in the stepwise selection procedure. 100% of the samples were classified correctly in the case of both the <63 µm and 63-125 µm fractions.

Table 2: The final composite signatures for discriminating individual spatial sediment sources using the <63 µm and 63–125 µm fractions.

Fraction	Tracer	Step	cumulative % of source samples classified correctly	% of source samples classified correctly by individual tracers
< 63 µm	Mg	1	84.5	84.5
	Zn	2	90.6	50.8
	Al	3	93.8	41.2
	Sr	4	95.5	56.4
	Ba	5	100	49.2
63–125 µm	Mg	1	76.9	76.9
	Sr	2	87.7	57.8
	Zn	3	94.6	40.3
	Na	4	100	46.9

For each particle size fraction, the canonical correlation value was 0.99, suggesting a strong relationship between the discriminant scores and the individual spatial source groups. Wilks' Lambda is a good measure of the ratio of intra-group differences to inter-group differences. The value of Wilks' lambda (0.001) of the first function for both particle size fractions indicated that 99% of the total variance among the spatial sediment source samples is explained by the final composite signatures. Scatterplots of the first and second discriminant functions associated with the final composite fingerprints for both fractions (Fig. 5) showed the powerful source discrimination provided by the final composite signatures.

Biplots of pairs of tracers in the final composite signatures were used as an additional means of assessing conservative behaviour (Fig. 6). These comparisons indicated no major tracer transformations during sediment routing in the study basin. In these biplots, the tracers plot along a line or within a similar space, which is a sign of the conservative behaviour of the tracers in question (Nosrati et al., 2019)

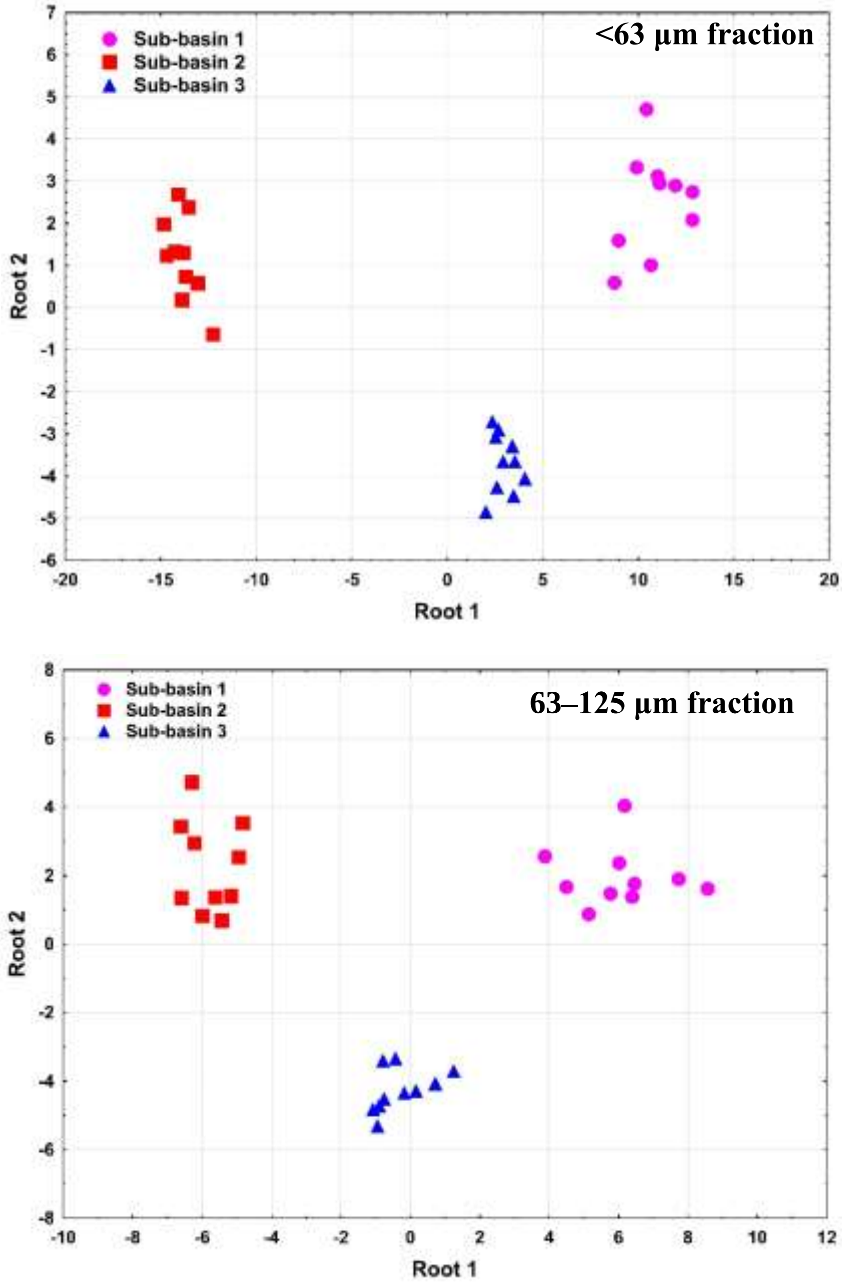

Fig. 5. Scatterplots of the first and second discriminant functions associated with the final composite fingerprints for the <63 μm and the 63–125 μm fractions.

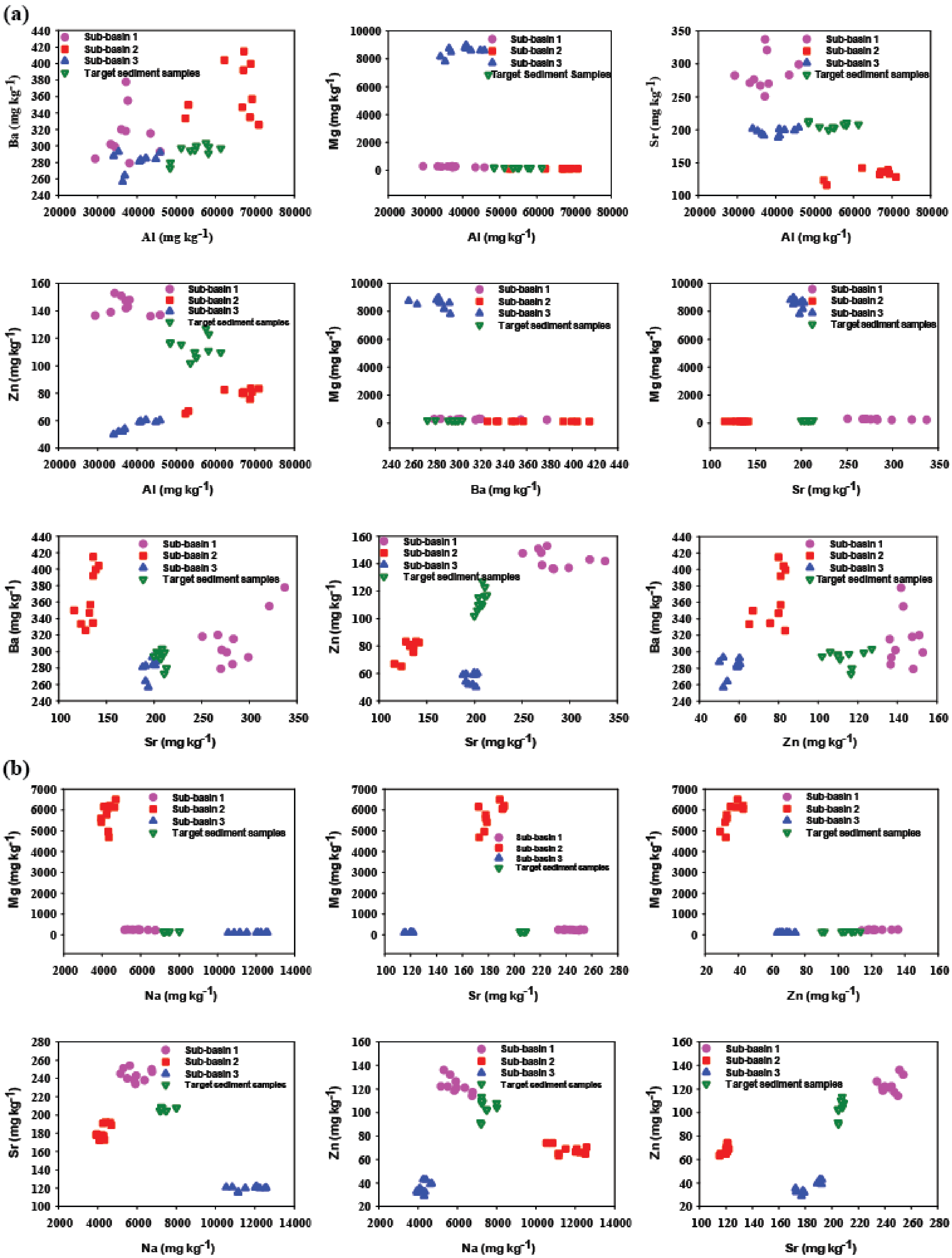
(a)
(b)
Sub-basin 1
Sub-basin 2
Sub-basin 3
Target sediment samples
Target Sediment Samples
Ba (mg kg-1)
Mg (mg kg-1)
Sr (mg kg-1)
Zn (mg kg-1)
Al (mg kg-1)
Na (mg kg-1)

Fig. 6. Biplots of selected tracers in the final composite fingerprints for discriminating and apportioning the spatial sediment sources using the two particle size fractions: a) the <63 µm fraction, and; b) the 63–125 µm fraction.

3.4. Spatial sediment source contributions

Using the final composite fingerprints, the relative contributions (with corresponding 5-95% uncertainty ranges) of tributary sub-catchment spatial sediment sources 1, 2 and 3 were estimated to be 51.9% (48.6-55.3), 48.0% (44.6-51.3) and 0.1% (0.0-0.2) for the <63 µm fraction compared with 68.2% (66.4- 69.8), 31.7% (30.1- 33.6) and 0.1% (0.0-0.2) for the 63-125 µm fraction. Estimation of source contributions using the relative likelihood function is illustrated in Fig. SI 2. These results suggested that tributary sub-basin 1 was the dominant spatial sediment source for both particle size fractions.

3.5. Correlation analysis between sediment loads and average PGA

Suspended sediment load data for 2020 at the outlet of the main basin were combined with the estimated spatial source proportions for each particle size fraction to estimate spatial sediment losses, and these, in turn, were plotted with PGA (Fig. 7). The correlations between sub-basin sediment loads and PGA were $r = 0.99$ for the <63 µm fraction and $r = 0.91$ for the 63–125 µm fraction. The correlations between sub-basin specific sediment loads (i.e., sediment load divided by sub-basin area) and PGA were $r = 0.68$ for the <63 µm fraction and $r = 0.99$ for the 63–125 µm fraction.

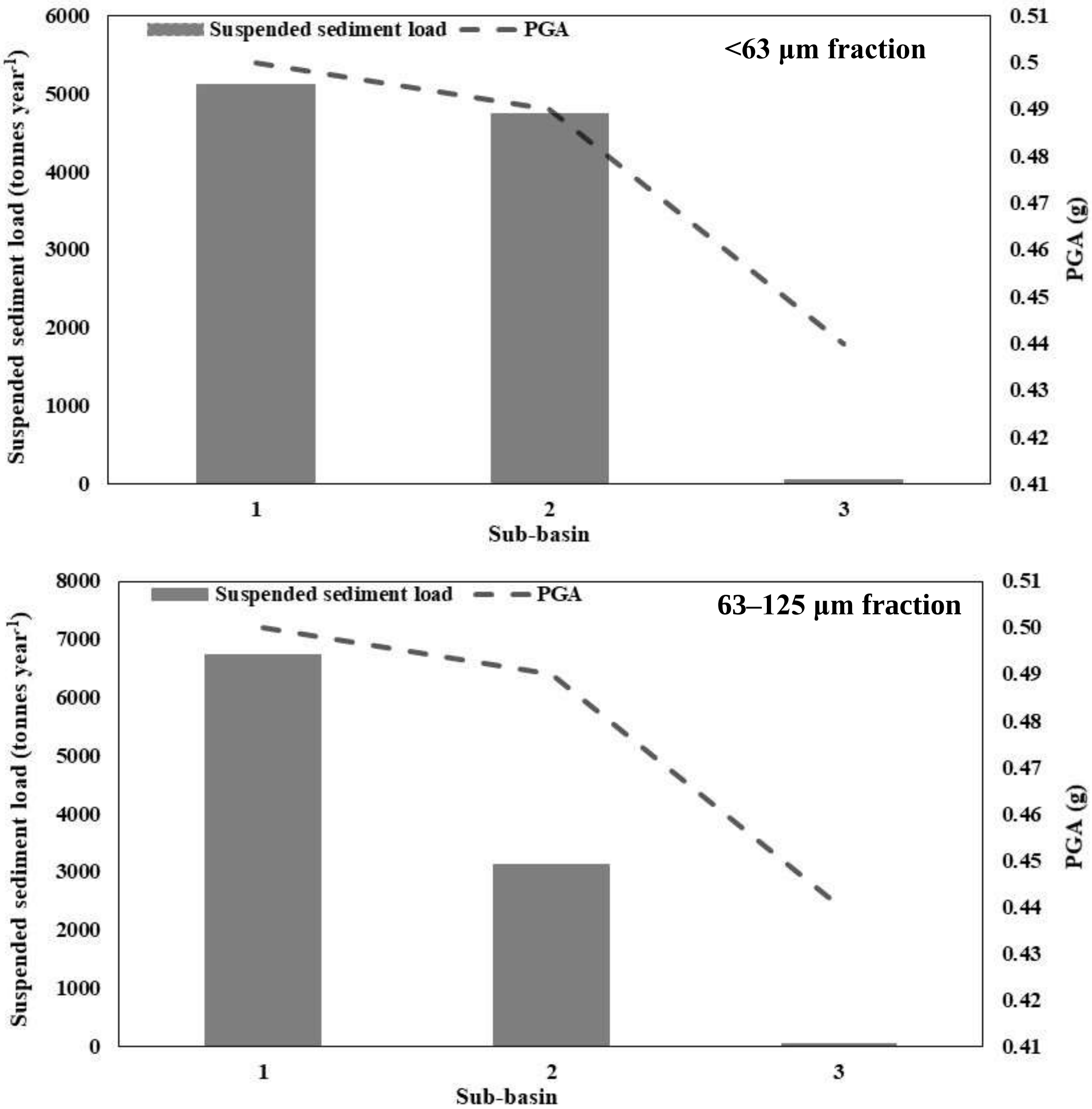

Fig. 7. Relationships between sub-basin spatial source sediment loads and average PGA for <63 µm and 63–125 µm fractions.

4. Discussion

4.1. Analysis of the impact of the largest earthquake event on suspended sediment load in the Talar drainage basin

According to the data presented in Fig. 8a and Fig.8b, in 1989, when the annual precipitation was 838 mm and no seismic event was recorded, the annual suspended sediment load was 5313 tonnes. In 1990, annual precipitation was 845.5 mm, and two seismic events occurred on January 20th and April 21st with respective magnitudes of M_w= 6 at a depth of 30 km and M_W = 4.5 at a depth of 29 km. The corresponding suspended sediment load in 1990 was 2199 tonnes. The impact of the largest earthquake with a magnitude of M_w= 6 was observed in 1991 and 1992. In 1991, only one event occurred on December 24th with the magnitude of M_w=3.5 at a depth of 38 km and the annual rainfall of 834 mm was similar to previous years. The corresponding suspended sediment load in 1991 was, however, much elevated at 14217 tonnes. According to the data presented in Fig. 8c, the mean depth of the earthquake in 1990 with 2 events was 29.5 km. This increase in suspended sediment load was due to the impact of the largest seismic event in1990, with a magnitude of M_w= 6, along with the effects of smaller earthquakes in 1990 and 1991, as well as the impacts of the depth factor and PGA. Shallow earthquakes occur at a depth of 0-30 km (Hejrani and Tkalčić, 2020). The earthquake in 1990 had the greatest depth and because of this, less energy propagated up to the land surface meaning that whilst this event was the largest seismic event in the region, it took more time to produce elevated sediment loads in the study region. The earthquake of 1990, because it was the biggest event in the Talar basin in recent years, has caused the most seismic activity in the region until today. According to the PGA map (Fig. 4), in the regions where the PGA has the highest values, it plays a significant role in the energy input to the bedrock and sediment production. PGA in the 1990 earthquake is estimated at 0.4-0.5 g. Given its magnitude, it has had a significant impact on the production of suspended sediments. Furthermore, during 1992, no seismic events occurred, but annual rainfall increased to 1256 mm, and the corresponding suspend sediment load was 21734 tonnes, which exceeded that in 1991. In 1993, with a decrease in annual precipitation to 876.5 mm and since no seismic events occurred, the annual suspended sediment load reduced to 1517 tonnes. Overall, the largest earthquakes with a relatively low depth during 1990-1991 are likely to have increased the sediment loads during 1991-1992. These results demonstrate a delay or lag-time observed between the frequency of earthquakes and elevated sediment loads.

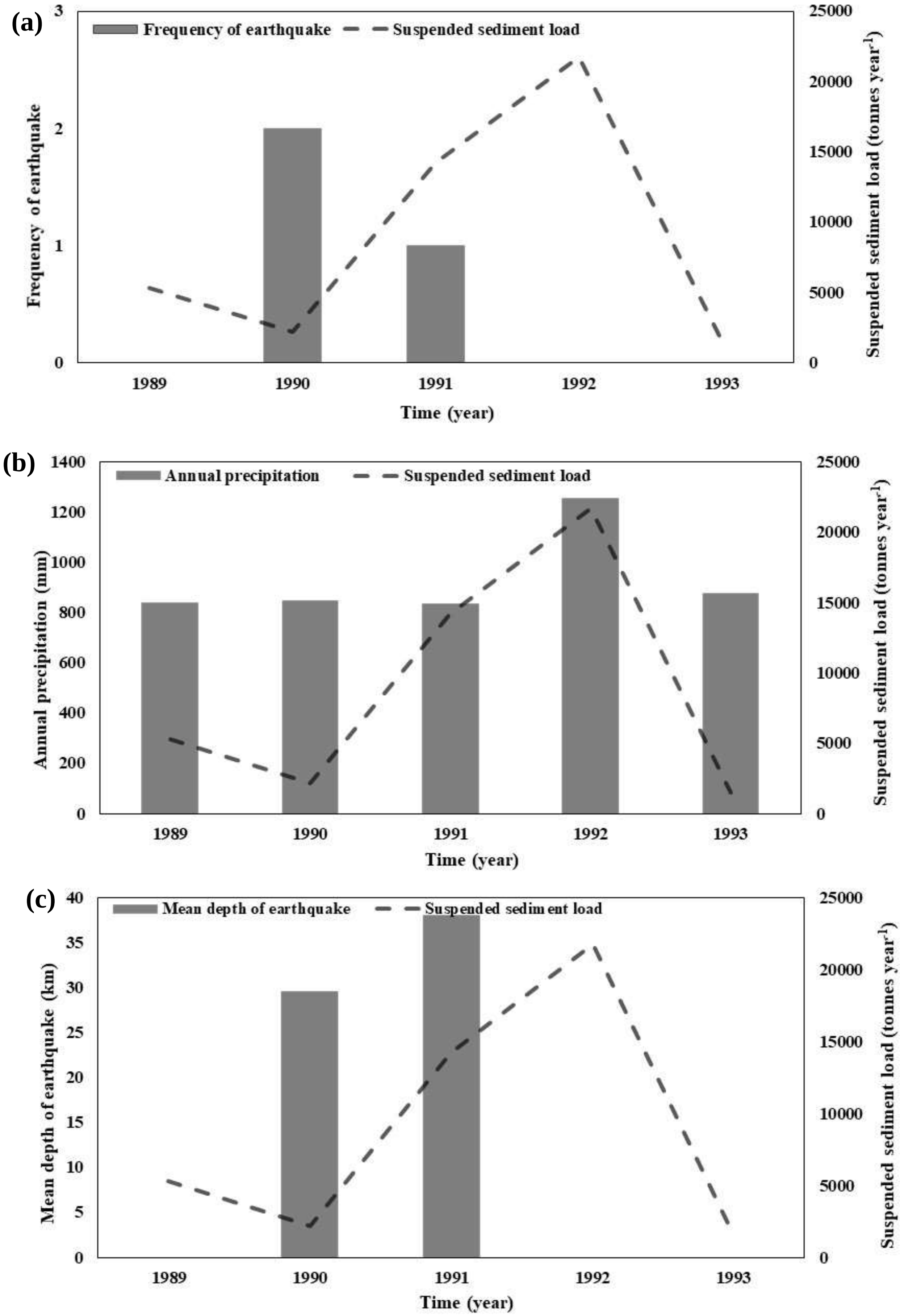
(a)
Frequency of earthquake
Suspended sediment load
Frequency of earthquake
Suspended sediment load (tonnes year^{-1})
Time (year)
1989
1990
1991
1992
1993
(b)
Annual precipitation
Suspended sediment load
Annual precipitation (mm)
Suspended sediment load (tonnes year^{-1})
Time (year)
(c)
Mean depth of earthquake
Suspended sediment load
Mean depth of earthquake (km)
Suspended sediment load (tonnes year^{-1})
Time (year)

Fig. 8. (a) The trend of the largest seismic events and suspended sediment loads (1989-1993); (b) annual precipitation, and; (c) mean depth of earthquakes.

4.2. Analysis of the effect of the frequency and magnitude of earthquakes on suspended sediment loads

The frequency and magnitude of earthquakes are two important controlling variables for the annual suspended sediment loads in the Talar drainage basin. The number of earthquakes with a magnitude exceeding 3.0 M_w recorded by seismographic networks since 2006 was assembled and the data were classified into three ranges comprising: ≥ $3.01 M_w$ (Fig. 9a); 3.01-4 M_w (Fig. 9b), and; 4.01-5 M_w (Fig. 9c).

The frequency of small earthquakes (Fig. 9a) appears to be an important controlling factor for suspended sediment loads (Malamud et al., 2004). According to Fig. 9a, the lowest frequency (n = 4) of earthquakes in 2013, combined with an annual precipitation of 1190 mm resulted in an annual suspended sediment load of 4416 tonnes. The highest frequency (n=18) of earthquakes in 2015, combined with a higher annual precipitation of 1102 mm resulted in a much elevated annual suspended sediment load of 17683 tonnes during the following year in 2016 (Fig. 9a). According to Fig. 9b and Fig 9c, in 2015, the frequency of earthquakes with magnitudes 3.01-4 M_w was 15 whereas there were three with magnitudes of 4.01-5 M_w Given the decrease in annual precipitation in 2015, the main controlling factor for elevated suspended sediment load was the frequency of earthquakes in 2007 and 2012, during which the respective annual suspended sediment loads were 28118 and 31879 tonnes. These two years experienced similar annual rainfall totals of 1230 mm and 1220 mm, but the higher frequency of earthquakes in 2012 generated a higher suspended sediment load. The depth of earthquakes during the years 2006 to 2020 is less than 10 km in most years. More specifically, from a total of 160 events over the period spanning 2006 to 2020, 114 events were at a depth of less than 10 km, 44 events were at a depth of 10 to 20 km, and 2 events were at a depth of more than 20 km. The mean depth of earthquakes is presented in Fig. 9d.

Linear regression analysis between suspended sediment load (SS) as the dependent variable and precipitation and frequency of earthquakes (FoE) as independent variables was performed for the years 2006 to 2020. Due to a lack of significance, the precipitation variable (p value = 0.06) was excluded from the analysis meaning that regression analysis was performed with only one independent variable (frequency of earthquakes) (p value = 0.02, r = 0.6. The final regression model can be expressed as: SS = 601+1325 FoE.

Therefore, based on the data presented in Fig. 8 and Fig. 9, both the frequency and magnitude of earthquakes, the depth factor and PGA, all impact the annual suspended sediment loads in the Talar drainage basin.

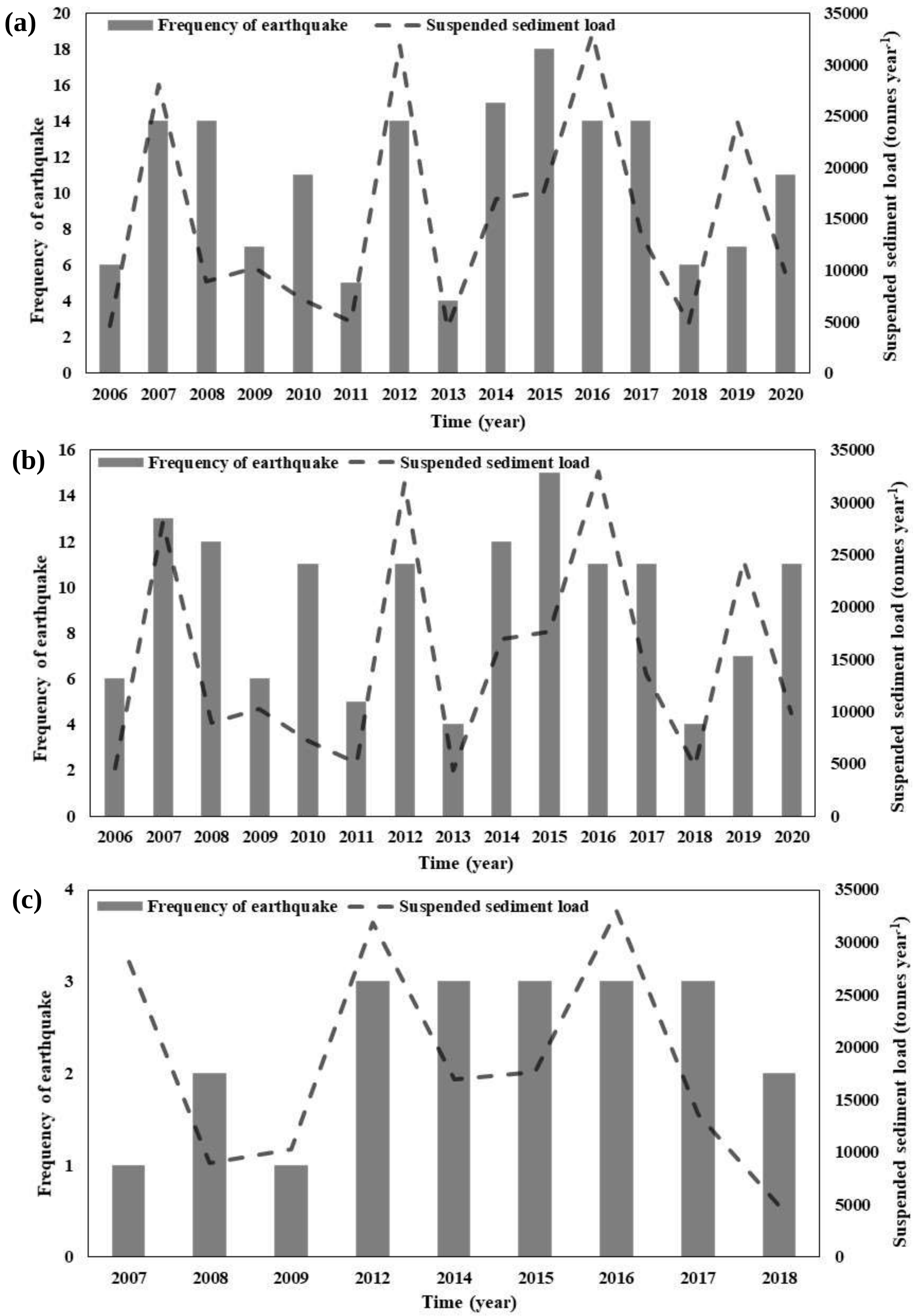
(a)
Frequency of earthquake
Suspended sediment load
Frequency of earthquake
Suspended sediment load (tonnes year^{-1})
Time (year)
2006 2007 2008 2009 2010 2011 2012 2013 2014 2015 2016 2017 2018 2019 2020
(b)
Frequency of earthquake
Suspended sediment load
Frequency of earthquake
Suspended sediment load (tonnes year^{-1})
Time (year)
2006 2007 2008 2009 2010 2011 2012 2013 2014 2015 2016 2017 2018 2019 2020
(c)
Frequency of earthquake
Suspended sediment load
Frequency of earthquake
Suspended sediment load (tonnes year^{-1})
Time (year)
2007 2008 2009 2012 2014 2015 2016 2017 2018

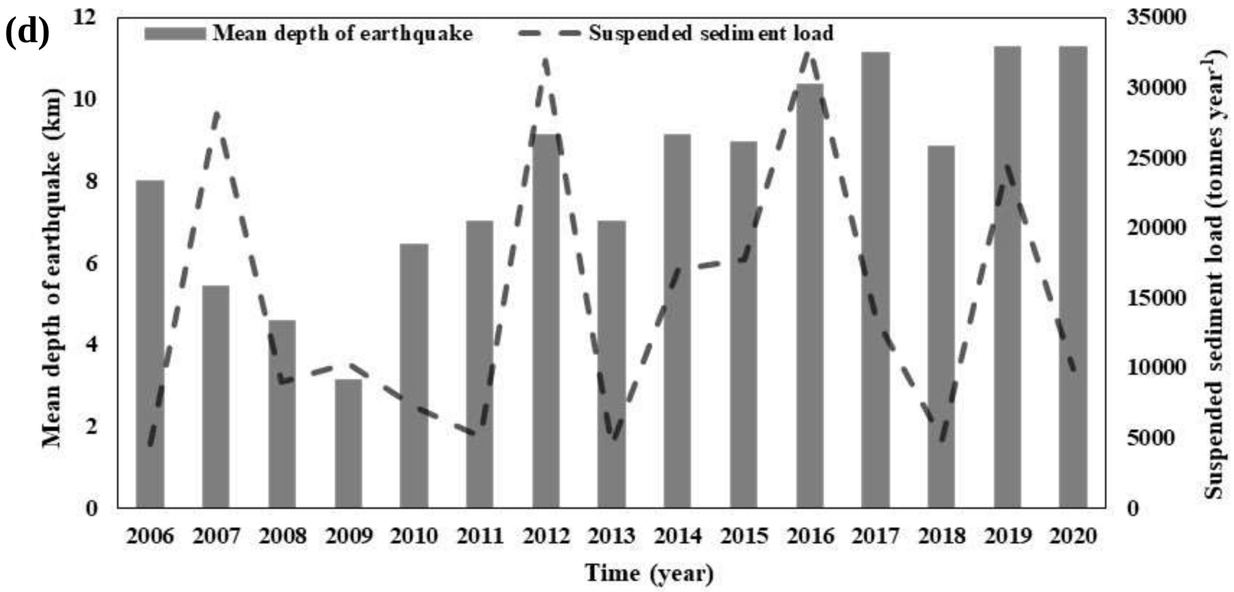

Fig. 9. The trends of the frequency of earthquakes and suspended sediment loads during the period 2006-2020: (a) earthquakes ≥ 3.01 Mw; (b) earthquakes 3.01-4 M_w; (c) earthquakes 4.01-5M_w, and; (d) mean depth of earthquakes.

4.3. Spatial sediment sources in the context of the seismic hazard map

Increased seismic activity has the propensity to elevate suspended sediment yields (Dadson et al., 2004a; Vanmaercke et al., 2014a). As shown in Fig. 4 in tributary sub-basin 1, 3 faults have elevated the PGA to 0.5 -0.6 g which exceeds that of both sub-basins 2 and 3. Furthermore, the descending order of PGA for the sub-basin spatial sources correlates with the predicted source contributions for both particle size fractions generated by MixSIR. Seismicity is therefore an important control on spatial sediment source contributions. In addition to the seismic effect, however, other factors (see section 4.4) can exert control on sediment production and delivery.

4.4. Spatial sediment sources in the context of geology, vegetation and lateral stream erosion

The main geological unit ($426.1\ km^2$ in sub-basin 1, $445\ km^2$ in sub-basin 2, and $180.5\ km^2$ in sub-basin 3) is the Shemshak Formation, which has rocky units (sandstone-conglomerate and shale) but also shale layers which are moderately erodible (Ahmadi and Feiznia, 2006; Momeni et al., 2014). In order to support a discussion of the impacts of other key factors that potentially control soil erosion and sediment loss, potential controls comprising the rainfall erosivity factor (R factor), erodibility factor (K factor), slope-length factor (LS factor), and cover management factor (C factor) (Fig. SI 3) were determined for each sub-basin (please see supplementary information for further details) and the correlation coefficients between specific sediment load (sediment load divided by area) and these key factors were investigated. For the <63 μm fraction, the coefficients for the R factor, K factor, LS factor, C factor, and PGA were estimated as -0.40, -0.81, 0.98, 0.70, and 0.83, compared to -0.82, -0.98, 0.93, 0.97, and 0.99 for the 63–125 μm fraction. These results suggest that seismic activity could help to simplify weathering processes and produce primary material and cause elevated erosion and sediment delivery. Sub-basin 1 is dominated by rangelands with an area of $692.5\ km^2$ (Fig. SI 4), and these are prone to overgrazing and erosion issues (Silburn et al., 2011), again helping to explain the higher contribution of this sub-basin. In contrast, in sub-basins 2 and 3, forest is dominant with corresponding respective areas of, $413.8\ km^2$ and $314.3\ km^2$. The area of eroded surfaces due to lateral stream erosion are $6.1\ km^2$ in $sub - basin\ 1$, $11.1\ km^2$ in $sub - basin\ 2$ and only $0.05\ km^2$ in $sub - basin\ 3$ (Iran Forests, Range and Watershed Management Organization; IFRWMO). So, the combination of higher seismic activity and maximum ground acceleration (0.6 g), an extensive presence of the Shemshak Formation, degraded rangeland and lateral stream erosion help to explain the higher contributions from tributary sub-basins 1 and 2.

In this study, PGA provided accurate assessment of the seismic activity of the sub-basins. Other recent studies (Antinao and Gosse, 2009; Dadson et al., 2004b; Hovius et al., 1997;

Howarth et al., 2012; Vanmaercke et al., 2014a) have also reported how seismic activity, landslides and rock movements are key factors in driving suspended sediment loads. Importantly, our PGA values are consistent with the values reported by previous studies (Khodaverdian et al., 2016; Mahsuli et al., 2019; Razaghian et al., 2018) in Iran.

5. Limitations of the work

Our results of investigating the effect of seismicity on spatial sediment sources and loads using the fingerprinting approach must be interpreted in the context of some limitations and uncertainties.

1- The lack of access to rainfall intensity data in the years when the earthquakes occurred is a limitation for investigating and verifying the effect of the earthquakes. For example: suspended sediment load in 1990 after two earthquake events was only half of that in 1989 when no seismic events were recorded. Although these two years experienced similar annual rainfall totals (Fig. 8), short intense storms occurred in 1989 but not in 1990. So, the lack of access to rainfall intensity data limits our ability to interpret our results in more depth.

2- Another limitation of the present study is related to the recording of earthquakes since, before 2006, the seismographic networks could not record events with magnitudes less than 3.5 Mw.

3- Given the challenges of deploying a more traditional hillslope source sampling strategy in the study area, an alternative confluence-based approach was deployed. Although this generated information on spatial sediment sources, it did not provide a basis for assembling information on sediment source types. Suspended sediment sampling during rainfall-runoff events also requires consideration of the temporal dimension. Here, it should be borne in mind that in our study, the contemporary sediment source contributions obtained were used to assess the impact of historical earthquakes on suspended sediment losses. An alternative approach would be to fingerprint historical sediment source contributions using sectioned and dated floodplain cores, but here, there are challenges with the non-conservative behaviour of tracers post deposition.

4- Our composite signatures were selected using statistical procedures and were not selected using any *a priori* understanding of the physico-chemical basis for discriminating the potential sediment sources identified in our study area. Whilst the majority of fingerprinting studies globally continue to use statistically-driven tracer selection procedures, the need to continue exploring and confirming the physico-chemical basis for discriminatory efficiency in different geographical environments continues to warrant further attention (Collins et al., 2020).

.

6. Conclusion

In this study, the relationship between seismicity and sediment sources and loads was investigated in the Talar drainage basin in northern Iran. The values of PGA vary in the Talar drainage basin. Due to several active faults in the region, the highest value of PGA (0.6 g) exists in sub-basins 1 and 2. The relative contributions of spatial sediment sources using the composite fingerprints suggested that sub-basin 1 is the main spatial source of the sampled sediments. The high correlation between sediment sources and the average PGA indicates the significant impact of seismicity on the production of sediments in the sub basins used to represent spatial sediment sources. Therefore earthquake attributes can affect suspended sediment loads in the study basin. A better understanding of the impact of seismicity on sediment production and delivery in the basin was obtained through the estimation of PGA and the analysis of events recorded with different magnitudes. Future investigations could target the effects of landslides on suspended sediment loss. Regardless, the results obtained in this study will be very useful for environmental planners to target management to reduce suspended sediment loads and preserve fluvial habitats.

Acknowledgements

This project was funded by a grant (grant number 600.871) from the research council of Shahid Beheshti University, Tehran, Iran. The contribution to this work by ALC was funded by UKRI-BBSRC (UK Research and Innovation Biotechnology and Biological Sciences Research Council) grant award BBS/E/C/000I0330.

References

Abrahamson, N., Atkinson, G., Boore, D., Bozorgnia, Y., Campbell, K., Chiou, B., Idriss, I.M., Silva, W., Youngs, R., 2008. Comparisons of the NGA Ground-Motion Relations. Earthquake Spectra 24(1), 45-66.

Ahmadi, H., Feiznia, S., 2006. Quaternary Formation. Theoretical and Practical Basis in Natural Resources. 2nd Edn., University of Tehran, Iran.

Aiello, A., Adamo, M., Canora, F., 2015. Remote sensing and GIS to assess soil erosion with RUSLE3D and USPED at river basin scale in southern Italy. CATENA 131, 174-185.

Akkar, S., Bommer, J.J., 2010. Empirical equations for the prediction of PGA, PGV, and spectral accelerations in Europe, the Mediterranean region, and the Middle East. Seismological Research Letters 81(2), 195-206.

Antinao, J.L., Gosse, J., 2009. Large rockslides in the Southern Central Andes of Chile (32–34.5°S): Tectonic control and significance for Quaternary landscape evolution. Geomorphology 104(3), 117-133.

Berberian, M., 1994. Natural hazards and the first earthquake catalogue of Iran. International Institute of Earthquake Engineers and Seismology.

Choi, S.-J., Jeon, J.S., Choi, J.-H., Kim, B., Ryoo, C.-R., Hong, D.-G., Chwae, U., 2014. Estimation of possible maximum earthquake magnitudes of Quaternary faults in the southern Korean Peninsula. Quaternary International 344, 53-63.

Collins, A., Zhang, Y., McChesney, D., Walling, D., Haley, S., Smith, P., 2012a. Sediment source tracing in a lowland agricultural catchment in southern England using a modified procedure combining statistical analysis and numerical modelling. Science of the Total Environment 414, 301-317.

Collins, A.L., Blackwell, M., Boeckx, P., Chivers, C.-A., Emelko, M., Evrard, O., Foster, I., Gellis, A., Gholami, H., Granger, S., Harris, P., Horowitz, A.J., Laceby, J.P., Martinez-Carreras, N., Minella, J., Mol, L., Nosrati, K., Pulley, S., Silins, U., da Silva, Y.J., Stone, M., Tiecher, T., Upadhayay, H.R., Zhang, Y., 2020. Sediment source fingerprinting: benchmarking recent outputs, remaining challenges and emerging themes. Journal of Soils and Sediments 20(12), 4160-4193.

Collins, A.L., Pulley, S., Foster, I.D.L., Gellis, A., Porto, P., Horowitz, A.J., 2017. Sediment source fingerprinting as an aid to catchment management: A review of the current state of knowledge and a methodological decision-tree for end-users. Journal of Environmental Management 194, 86-108.

Collins, A.L., Walling, D.E., 2002. Selecting fingerprint properties for discriminating potential suspended sediment sources in river basins. Journal of Hydrology 261(1), 218-244.

Collins, A.L., Walling, D.E., 2004. Documenting catchment suspended sediment sources: problems, approaches and prospects. Progress in Physical Geography 28, 159 - 196.

Collins, A.L., Walling, D.E., Leeks, G.J.L., 1997a. Sediment sources in the Upper Severn catchment: a fingerprinting approach. Hydrol. Earth Syst. Sci. 1(3), 509-521.

Collins, A.L., Walling, D.E., Leeks, G.J.L., 1997b. Source type ascription for fluvial suspended sediment based on a quantitative composite fingerprinting technique. CATENA 29(1), 1-27.

Collins, A.L., Zhang, Y., McChesney, D., Walling, D.E., Haley, S.M., Smith, P., 2012b. Sediment source tracing in a lowland agricultural catchment in southern England using a modified procedure combining statistical analysis and numerical modelling. Science of The Total Environment 414, 301-317.

Cornell, C.A., 1968. Engineering seismic risk analysis. Bulletin of the Seismological Society of America 58(5), 1583-1606.

Cornell, C.A., Howells, D., Haigh, I., Taylor, C., 1971. Probabilistic analysis of damage to structures under seismic loads. Dynamic waves in civil engineering, 473-488.

Dadson, S., Hovius, N., Chen, H., Dade, W., Lin, J.-C., Hsu, M.-L., Lin, C.-W., Horng, M.-J., Chen, T.-C., Milliman, J., Stark, C., 2004a. Earthquake-driven increase in sediment delivery from an active mountain belt. Geology 32.

Dadson, S.J., Hovius, N., Chen, H., Dade, W.B., Lin, J.-C., Hsu, M.-L., Lin, C.-W., Horng, M.-J., Chen, T.-C., Milliman, J., Stark, C.P., 2004b. Earthquake-triggered increase in sediment delivery from an active mountain belt. Geology 32(8), 733-736.

Eluyemi, A.A., Ibitoye, F.I., Baruah, S., 2020. Preliminary analysis of probabilistic seismic hazard assessment for nuclear power plant site in nigeria. Scientific African 8, e00409.

Evrard, O., Navratil, O., Ayrault, S., Ahmadi, M., Némery, J., Legout, C., Lefèvre, I., Poirel, A., Bonté, P., Esteves, M., 2011. Combining suspended sediment monitoring and fingerprinting to determine the spatial origin of fine sediment in a mountainous river catchment. Earth Surface Processes and Landforms 36(8), 1072-1089.

Gardner, J., Knopoff, L., 1974. Is the sequence of earthquakes in Southern California, with aftershocks removed, Poissonian? Bulletin of the seismological society of America 64(5), 1363-1367.

Ghasemi, H., Zare, M., Fukushima, Y., Koketsu, K., 2009a. An empirical spectral ground-motion model for Iran. Journal of Seismology 13(4), 499-515.

Ghasemi, H., Zare, M., Fukushima, Y., Sinaeian, F., 2009b. Applying empirical methods in site classification, using response spectral ratio (H/V): A case study on Iranian strong motion network (ISMN). Soil Dynamics and Earthquake Engineering 29(1), 121-132.

Golosov, V., Tsyplenkov, A., 2021. Factors Controlling Contemporary Suspended Sediment Yield in the Caucasus Region. Water 13(22), 3173.

Gutenberg, B., Richter, C.F., 1944. Frequency of earthquakes in California. Bulletin of the Seismological society of America 34(4), 185-188.

Hejrani, B., Tkalčić, H., 2020. Resolvability of the centroid-moment-tensors for shallow seismic sources and improvements from modeling high-frequency waveforms. Journal of Geophysical Research: Solid Earth 125(7), e2020JB019643.

Horowitz, A.J., Elrick, K.A., 1987. The relation of stream sediment surface area, grain size and composition to trace element chemistry. Applied geochemistry 2(4), 437-451.

Hovius, N., Meunier, P., Lin, C.-W., Chen, H., Chen, Y.-G., Dadson, S., Horng, M.-J., Lines, M., 2011. Prolonged seismically induced erosion and the mass balance of a large earthquake. Earth and Planetary Science Letters 304(3), 347-355.

Hovius, N., Stark, C.P., Allen, P.A., 1997. Sediment flux from a mountain belt derived by landslide mapping. Geology 25(3), 231-234.

Howarth, J.D., Fitzsimons, S.J., Norris, R.J., Jacobsen, G.E., 2012. Lake sediments record cycles of sediment flux driven by large earthquakes on the Alpine fault, New Zealand. Geology 40(12), 1091-1094.

Jenner, G.A., Longerich, H.P., Jackson, S.E., Fryer, B.J., 1990. ICP-MS — A powerful tool for high-precision trace-element analysis in Earth sciences: Evidence from analysis of selected U.S.G.S. reference samples. Chemical Geology 83(1), 133-148.

Khodaverdian, A., Zafarani, H., Rahimian, M., Dehnamaki, V., 2016. Seismicity Parameters and Spatially Smoothed Seismicity Model for Iran. Bulletin of the Seismological Society of America 106(3), 1133-1150.

Kijko, A., Sellevoll, M.A., 1992. Estimation of earthquake hazard parameters from incomplete data files. Part II. Incorporation of magnitude heterogeneity. Bulletin of the Seismological Society of America 82(1), 120-134.

Kijko, A., Smit, A., 2012. Extension of the Aki-Utsu b-Value Estimator for Incomplete Catalogs. Bulletin of the Seismological Society of America 102(3), 1283-1287.

Koons, P.O., Upton, P., Barker, A.D., 2012. The influence of mechanical properties on the link between tectonic and topographic evolution. Geomorphology 137(1), 168-180.

Lamba, J., Karthikeyan, K.G., Thompson, A.M., 2015. Apportionment of suspended sediment sources in an agricultural watershed using sediment fingerprinting. Geoderma 239-240, 25-33.

Lee, W.H., Jennings, P., Kisslinger, C., Kanamori, H., 2002. International handbook of earthquake & engineering seismology, Part A. Elsevier.

Mahsuli, M., Rahimi, H., Bakhshi, A., 2019. Probabilistic seismic hazard analysis of Iran using reliability methods. Bulletin of Earthquake Engineering 17(3), 1117-1143.

Malamud, B.D., Turcotte, D.L., Guzzetti, F., Reichenbach, P., 2004. Landslides, earthquakes, and erosion. Earth and Planetary Science Letters 229(1), 45-59.

McGuire, R.K., 1976. FORTRAN computer program for seismic risk analysis. 76-67.

Minella, J.P., Clarke, R.T., Merten, G.H., Walling, D.E., 2008. Sediment source fingerprinting: testing hypotheses about contributions from potential sediment sources, Sediment Dynamics in Changing Environments-2008 Symposium of the International Commission on Continental Erosion, ICCE, pp. 31-37.

Mohammadi, M., Khaledi Darvishan, A.K., Spalevic, V., Dudic, B., Billi, P., 2021. Analysis of the Impact of Land Use Changes on Soil Erosion Intensity and Sediment Yield Using the IntErO Model in the Talar Watershed of Iran. Water 13(6), 881.

Molnar, P., Anderson, R.S., Anderson, S.P., 2007. Tectonics, fracturing of rock, and erosion. Journal of Geophysical Research: Earth Surface 112(F3).

Momeni, M., Moeini, A., Ahmadi, H., 2014. A Study of the impacts of different characteristics of geological formations in producing various erosion forms (Case Study: Watershed basin Hio and Shalamzar). Journal of Biodiversity and Environmental Sciences (JBES) 5(3), 86-94.

Monterroso Juárez, D.A., 2003. Statistical Seismology Studies in Central America: b-value, seismic hazard and seismic quiescence: Acta Universitatis Upsaliensis.

Moore, J.W., Semmens, B.X., 2008. Incorporating uncertainty and prior information into stable isotope mixing models. Ecology Letters 11(5), 470-480.

Motha, J., Wallbrink, P., Hairsine, P., Grayson, R., 2003. Determining the sources of suspended sediment in a forested catchment in southeastern Australia. Water resources research 39(3).

Nadeu, E., de Vente, J., Martínez-Mena, M., Boix-Fayos, C., 2011. Exploring particle size distribution and organic carbon pools mobilized by different erosion processes at the catchment scale. Journal of Soils and Sediments 11, 667-678.

Nosrati, K., 2017. Ascribing soil erosion of hillslope components to river sediment yield. Journal of Environmental Management 194, 63-72.

Nosrati, K., Akbari-Mahdiabad, M., Ayoubi, S., Degos, E., Koubansky, A., Coquatrix, Q., Pulley, S., Collins, A.L., 2020. Storm dust source fingerprinting for different particle size fractions using colour and magnetic susceptibility and a Bayesian un-mixing model. Environmental Science and Pollution Research 27, 31578-31594.

Nosrati, K., Collins, A.L., 2019a. Fingerprinting the contribution of quarrying to fine-grained bed sediment in a mountainous catchment, Iran. River Research and Applications 35(3), 290-300.

Nosrati, K., Collins, A.L., 2019b. Investigating the importance of recreational roads as a sediment source in a mountainous catchment using a fingerprinting procedure with different multivariate statistical techniques and a Bayesian un-mixing model. Journal of Hydrology 569, 506-518.

Nosrati, K., Collins, A.L., Madankan, M., 2018. Fingerprinting sub-basin spatial sediment sources using different multivariate statistical techniques and the Modified MixSIR model. CATENA 164, 32-43.

Nosrati, K., Fathi, Z., Collins, A.L., 2019. Fingerprinting sub-basin spatial suspended sediment sources by combining geochemical tracers and weathering indices. Environmental Science and Pollution Research 26(27), 28401-28414.

Nosrati, K., Govers, G., Semmens, B.X., Ward, E.J., 2014. A mixing model to incorporate uncertainty in sediment fingerprinting. Geoderma 217-218, 173-180.

Nuannin, P., Kulhanek, O., Persson, L., 2005. Spatial and temporal b value anomalies preceding the devastating off coast of NW Sumatra earthquake of December 26, 2004. Geophysical Research Letters 32(11).

Ommi, S., Zafarani, H., 2016. Analyses of seismicity parameters of the August 11th, 2012, Ahar-Varzaghan earthquakes in north-western Iran. Scientia Iranica 23(2), 449-459.

Owens, P.N., Batalla, R.J., Collins, A.J., Gomez, B., Hicks, D.M., Horowitz, A.J., Kondolf, G.M., Marden, M., Page, M.J., Peacock, D.H., Petticrew, E.L., Salomons, W., Trustrum, N.A., 2005. Fine-grained sediment in river systems: environmental significance and management issues. River Research and Applications 21(7), 693-717.

Palazón, L., Navas, A., 2017. Variability in source sediment contributions by applying different statistic test for a Pyrenean catchment. Journal of Environmental Management 194, 42-53.

Portenga, E.W., Bierman, P.R., 2011. Understanding Earth's eroding surface with 10 Be.

Pulley, S., Foster, I., Antunes, P., 2015. The uncertainties associated with sediment fingerprinting suspended and recently deposited fluvial sediment in the Nene river basin. Geomorphology 228, 303-319.

Pulley, S., Foster, I., Collins, A.L., 2017. The impact of catchment source group classification on the accuracy of sediment fingerprinting outputs. Journal of Environmental Management 194, 16-26.

Raigani, Z.M., Nosrati, K., Collins, A.L., 2019. Fingerprinting sub-basin spatial sediment sources in a large Iranian catchment under dry-land cultivation and rangeland farming: Combining geochemical tracers and weathering indices. Journal of Hydrology: Regional Studies 24, 100613.

Razaghian, G., Beitollahi, A., Pourkermani, M., Arian, M., 2018. Determining seismotectonic provinces based on seismicity coefficients in Iran. Journal of Geodynamics 119, 29-46.

Salamat, M., Zöller, G., Amini, M., 2019. Prediction of the Maximum Expected Earthquake Magnitude in Iran: From a Catalog with Varying Magnitude of Completeness and Uncertain Magnitudes. Pure and Applied Geophysics 176(8), 3425-3438.

Schorlemmer, D., Neri, G., Wiemer, S., Mostaccio, A., 2003. Stability and significance tests for b-value anomalies: Example from the Tyrrhenian Sea. Geophysical Research Letters - GEOPHYS RES LETT 30.

Shahvar, M.P., Zare, M., Castellaro, S., 2013. A unified seismic catalog for the Iranian plateau (1900–2011). Seismological Research Letters 84(2), 233-249.

Silburn, D., Carroll, C., Ciesiolka, C.A.A., deVoil, R.C., Burger, P., 2011. Hillslope runoff and erosion on duplex soils in grazing lands in semi-arid central Queensland. I. Influences of cover, slope, and soil. Soil Research 49, 105-117.
Smith, W.D., 1981. The b-value as an earthquake precursor. Nature 289(5794), 136-139.
Soghrat, M.R., Khaji, N., Zafarani, H., 2012. Simulation of strong ground motion in northern Iran using the specific barrier model. Geophysical Journal International 188(2), 645-679.
StatSoft, 2008. STATISTICA: [Data Analysis Software System], Version 8.0 for Windows Update. (p. StatSoft, Inc.).
Taylor, A., Blake, W., Smith, H., Mabit, L., Keith-Roach, M., 2013. Assumptions and challenges in the use of fallout beryllium-7 as a soil and sediment tracer in river basins. Earth-science reviews 126, 85-95.
Tiecher, T., Minella, J.P.G., Evrard, O., Caner, L., Merten, G.H., Capoane, V., Didoné, E.J., dos Santos, D.R., 2018. Fingerprinting sediment sources in a large agricultural catchment under no-tillage in Southern Brazil (Conceição River). Land Degradation & Development 29(4), 939-951.
Tsukakoshi, Y., Shimazaki, K., 2008. Decreased b-value prior to the M 6.2 Northern Miyagi, Japan, earthquake of 26 July 2003. Earth, Planets and Space 60(9), 915-924.
Vahidifard, H., Zafarani, H., Sabbagh-Yazdi, S.-R., Hadian, M., 2017. Seismic hazard analysis using simulated ground-motion time histories: The case of the Sefidrud dam, Iran. Soil Dynamics and Earthquake Engineering 99, 20-34.
Vanmaercke, M., Ardizzone, F., Rossi, M., Guzzetti, F., 2017. Exploring the effects of seismicity on landslides and catchment sediment yield: An Italian case study. Geomorphology 278, 171-183.
Vanmaercke, M., Kettner, A.J., Eeckhaut, M.V.D., Poesen, J., Mamaliga, A., Verstraeten, G., Rãdoane, M., Obreja, F., Upton, P., Syvitski, J.P.M., Govers, G., 2014a. Moderate seismic activity affects contemporary sediment yields. Progress in Physical Geography: Earth and Environment 38(2), 145-172.
Vanmaercke, M., Obreja, F., Poesen, J., 2014b. Seismic controls on contemporary sediment export in the Siret river catchment, Romania. Geomorphology 216, 247-262.
Vanmaercke, M., Poesen, J., Govers, G., Verstraeten, G., 2015. Quantifying human impacts on catchment sediment yield: A continental approach. Global and Planetary Change 130, 22-36.
Walling, D.E., 2013. The evolution of sediment source fingerprinting investigations in fluvial systems. Journal of Soils and Sediments 13(10), 1658-1675.
Walling, D.E., Golosov, V., Olley, J.M., 2013. Introduction to the special issue 'Tracer Applications in Sediment Research'. Hydrological Processes 27.
Wang, Z., Govers, G., Steegen, A., Clymans, W., Van den Putte, A., Langhans, C., Merckx, R., Van Oost, K., 2010. Catchment-scale carbon redistribution and delivery by water erosion in an intensively cultivated area. Geomorphology 124(1-2), 65-74.
Wiemer, S., Wyss, M., 1997. Mapping the frequency-magnitude distribution in asperities: An improved technique to calculate recurrence times? Journal of Geophysical Research: Solid Earth 102(B7), 15115-15128.
Wiemer, S., Wyss, M., 2000. Minimum Magnitude of Completeness in Earthquake Catalogs: Examples from Alaska, the Western United States, and Japan. Bulletin of the Seismological Society of America 90(4), 859-869.
Wilkinson, S.N., Hancock, G.J., Bartley, R., Hawdon, A.A., Keen, R.J., 2013. Using sediment tracing to assess processes and spatial patterns of erosion in grazed rangelands, Burdekin River basin, Australia. Agriculture, Ecosystems & Environment 180, 90-102.
Wu, Y.-M., Chiao, L.-Y., 2006. Seismic Quiescence before the 1999 Chi-Chi, Taiwan, Mw 7.6 Earthquake. Bulletin of the Seismological Society of America 96(1), 321-327.
Wyss, M., Stefansson, R., 2006. Nucleation Points of Recent Mainshocks in Southern Iceland, Mapped by b-Values. Bulletin of the Seismological Society of America 96(2), 599-608.

Zare, M., Panagopoulos, T., Loures, L., 2017. Simulating the impacts of future land use change on soil erosion in the Kasilian watershed, Iran. Land Use Policy 67, 558-572.
Zarrineghbal, A., Zafarani, H., Rahimian, M., 2021. Towards an Iranian national risk-targeted model for seismic hazard mapping. Soil Dynamics and Earthquake Engineering 141, 106495.
Zhou, M., Deng, J., Lin, Y., Belete, M., Wang, K., Comber, A., Huang, L., Gan, M., 2019. Identifying the effects of land use change on sediment export: Integrating sediment source and sediment delivery in the Qiantang River Basin, China. Science of The Total Environment 686, 38-49.